SEARCH FOR NEW LIGHT SCALAR BOSONS PRODUCED IN ASSOCIATION WITH A BOTTOM-QUARK AND DECAYING TO TWO TAU LEPTONS

by

PETER RADLOFF

A DISSERTATION

Presented to the Department of Physics
and the Graduate School of the University of Oregon
in partial fulfillment of the requirements
for the degree of
Doctor of Philosophy

June 2016

DISSERTATION APPROVAL PAGE

Student: Peter Radloff

Title: Search for New Light Scalar Bosons Produced in Association with a Bottom-Quark and Decaying to Two Tau Leptons

This dissertation has been accepted and approved in partial fulfillment of the requirements for the Doctor of Philosophy degree in the Department of Physics by:

Stephanie Majewski	Chair
David Strom	Advisor
Spencer Chang	Core Member
Michael Kellman	Institutional Representative

and

Scott L Pratt	Dean of the Graduate School

Original approval signatures are on file with the University of Oregon Graduate School.

Degree awarded June 2016

DISSERTATION ABSTRACT

Peter Radloff

Doctor of Philosophy

Department of Physics

June 2016

Title: Search for New Light Scalar Bosons Produced in Association with a Bottom-Quark and Decaying to Two Tau Leptons

A search for new neutral scalar bosons produced in association with a bottom-quark is performed. The analysis uses data acquired with proton-proton collisions at a center-of-mass energy of 8 TeV and observed with the ATLAS detector at the LHC, corresponding to 20.3 fb^{-1} of integrated luminosity. The search focuses on scalar boson decays into tau lepton pairs, where each decays leptonically ($\tau \rightarrow l\nu_{\tau}\bar{\nu_{l}}$) resulting in one muon, one electron and four neutrinos. No significant excess is observed and upper limits on the signal strength are determined as a function of scalar boson mass.

CURRICULUM VITAE

NAME OF AUTHOR: Peter Radloff

GRADUATE AND UNDERGRADUATE SCHOOLS ATTENDED:

University of Oregon, Eugene, OR
University of Minnesota, Minneapolis, MN

DEGREES AWARDED:

Doctor of Philosophy, Physics, 2016, University of Oregon
Bachelor of Science, Physics, 2009, University of Minnesota

AREAS OF SPECIAL INTEREST:

Experimental Physics Beyond the Standard Model
Data Analysis and Tool Development
Systems Automation

PROFESSIONAL EXPERIENCE:

Graduate Research Assistant, University of Oregon, 2010 - 2016
Graduate Teaching Fellow, University of Oregon, 2009 - 2010

PUBLICATIONS:

ATLAS Collaboration. Identification and energy calibration of hadronically decaying tau leptons with the ATLAS experiment in pp collisions at $\sqrt{s}$=8 TeV. Eur. Phys. J. C75 (2015) 303, 2014.

Peter Radloff for the ATLAS Collaboration. The ATLAS hadronic tau trigger. Journal of Instrumentation. 8(03) C03009, 2013.

TABLE OF CONTENTS

Chapter Page

I. INTRODUCTION 1

II. THEORY 3

Introduction 3

The Standard Model 3

Beyond The Standard Model 8

III. THE LHC AND ATLAS 12

The Large Hadron Collider 12

The ATLAS Detector 12

ATLAS Detector Response 18

Simulation 23

IV. SEARCH FOR LOW-MASS $\Phi \rightarrow \tau_e\tau_\mu$ PRODUCED IN ASSOCIATION WITH A BOTTOM-JET 25

Introduction 25

Data Samples 25

Object Selection 27

Background Estimation 31

Chapter Page

Event Selection 33

Systematic Uncertainty 52

Results 57

V. CONCLUSION 62

REFERENCES CITED 63

LIST OF FIGURES

Figure Page

1. The CKM matrix describing quark flavor mixing [46]. 11
2. Magnitudes of CKM matrix [46]. 11
3. LEP limit result [8]. 11
4. An illustration of the ATLAS detector [5]. 14
5. An illustration of the inner detector of ATLAS [5]. 14
6. An illustration of the calorimeters of ATLAS [5]. 17
7. An illustration of the muon system of ATLAS [5]. 17
8. An illustration of the magnet systems of ATLAS [47]. 24
9. Di-muon invariant mass distribution after basic selection. 36
10. Event kinematics after basic selection. 37
11. Kinematic distributions of leptons after basic selection. 38
12. Jet related distributions after basic selection. 39
13. Event kinematics after basic selection. 40
14. Sum $E_{\mathrm{T}} \times M_{\mathrm{T}}(\vec{E}_{\mathrm{T}}^{\mathrm{miss}}, \mu)+M_{\mathrm{T}}(\vec{E}_{\mathrm{T}}^{\mathrm{miss}}, \mathrm{e})$ after basic selection. 41
15. Kinematic distributions of leptons after Z+jets validation selection. 42
16. Jet related distributions after Z+jets validation selection. 43
17. Event kinematics after Z+jets validation selection. 44
18. Kinematic distributions of leptons after $t\bar{t}$ validation selection. 45
19. Jet related distributions after $t\bar{t}$ validation selection. 46
20. Event kinematics after $t\bar{t}$ validation selection. 47
21. Kinematic distributions of leptons after multi-jet validation selection. . . 49
22. Jet related distributions after multi-jet validation selection. 50

Figure Page

23. Event kinematics after multi-jet validation selection. 51

24. Kinematic distributions of leptons after signal selection. 54

25. Jet related distributions after signal selection. 55

26. Event kinematics after signal selection. 56

27. 95% confidence upper limits. 61

LIST OF TABLES

Table Page

1. Fermions of the Standard Model [46]. 4
2. Bosons of the Standard Model [46]. 4
3. Requirements defining fiducial signal region. 26
4. Cross-sections for simulated samples 27
5. A summary of muon requirements. 28
6. A summary of electron requirements. 28
7. Summary of jet requirements. 28
8. Event counts after basic selection. 34
9. Event counts after Z+jets validation selection. 35
10. Event counts after $t\bar{t}$ validation selection. 36
11. Event counts after multi-jet validation selection. 48
12. Event counts after signal selection. 53
13. Summary of effect of systematic uncertainties. 53
14. Event counts per mass window after signal selection. 60
15. Efficiency per mass point as a function of Φ p_T. 60

CHAPTER I

INTRODUCTION

The field of high energy particle physics seeks to probe and understand nature's tumultuous and vibrant fabric at the smallest length scales. The Standard Model [36] (SM), developed in the 1970s, describes the interactions of particles known as fermions, via force intermediaries known as gauge bosons. The SM admits two classes of fermions: leptons and quarks, of which there are three mass hierarchal doublets. All of these fermions were experimentally observed by 2000. The gauge bosons, with the exception of the Higgs boson which is responsible for electroweak symmetry breaking, were observed by the mid 1980s. The Large Hadron Collider (LHC) at the European Organization for Nuclear Reseach (CERN) pushed the energy frontier, by making much harder collisions of subatomic particles and accumulating vast amounts of data resulting from these collisions. In 2012, the ATLAS and CMS experiments, at the LHC, jointly announced the discovery of the Higgs boson [7, 22]. Since then the result has been confirmed and it appears consistent with the SM.

The SM works quite well, but it is in need of extension to explain some theoretical problems and emperical observations. In the context of this thesis, an extension which results in additional scalar bosons is explored. Such an extension can be found, for example, in two-higgs doublet models (2HDM), in which a second Higgs doublet is added to the SM. This results in two charge-parity (CP) even neutral bosons (one identified as the discovered Higgs), one CP odd neutral boson, and two charged bosons. The charge-parity operator acting on a CP-even (CP-odd) eigenstate returns the positive (negative) of the eigenstate.

This thesis presents the search for a new scalar boson. The new scalar boson is searched for in association with a bottom-quark jet and in the mode decaying to two taus. The fully leptonic tau decay mode ($\tau_e \to e\nu_\tau\bar{\nu_e}$, $\tau_\mu \to \mu\nu_\tau\bar{\nu_\mu}$) is used. This final state is of interest because the backgrounds at the LHC are smaller than that of the corresponding hadronic final states of the tau lepton.

Chapter II describes the theoretical motivation. Chapter III describes the LHC, the ATLAS detector, and the ATLAS event data. Chapter IV describes the new physics search. Chapter V summarizes the result and concludes the dissertation.

CHAPTER II

THEORY

Introduction

This chapter discusses the Standard Model (SM) of particle physics. It also discusses shortcomings of the SM and an extension including new physics relevant for the analysis presented in this thesis.

The Standard Model

The SM is based on a quantum field theory (QFT) called a "Yang-Mills" theory [52]. Fermions interact via gauge bosons and those interactions are described by gauge invariance of certain Lie groups.

The gauge invariance of the $\mathrm{SU(3)_C}$ Lie group gives rise to the gluon fields (G^{α}_{μ},$\alpha \in \{ 1, 2, \ldots, 8 :\}$) which mediate colored interactions. $\mathrm{SU(2)_L} \times \mathrm{U(1)_Y}$ gives rise to the electroweak boson fields (W^1_μ, W^2_μ, W^3_μ, B_μ). Through the Higgs mechanism (described in Section 2.2) electroweak symmetry is broken ($\mathrm{SU(2)_L} \times \mathrm{U(1)_Y} \rightarrow \mathrm{U(1)_{EM}}$) resulting in a Higgs boson and granting the weak bosons and fermions mass.

A summary of the fermions can be found in Table 1 and a summary of the bosons in Figure 2.

Quantum Electrodynamics

Quantum electrodynamics (QED) describes the interaction of charged fermions mediated by the neutral massless photon. The coupling constant of the

Particle	Mass (MeV)	Charge
Leptons		
electron (e)	0.51	-1
electron neutrino (ν_e)	≈0	0
muon (μ)	105	-1
muon neutrino (ν_μ)	≈0	0
tau (τ)	1,777	-1
tau neutrino (ν_τ)	≈0	0
Quarks		
up (u)	1.5-3.0	+2/3
down (d)	4-6.5	-1/3
charm (c)	1,275	+2/3
strange (s)	95	-1/3
top (t)	173,210	+2/3
bottom (b)	4,180	-1/3

TABLE 1. Fermions of the Standard Model [46].

Particle	Mass (GeV)	Charge	Spin
photon (γ)	0	0	1
gluon (g)	0	0	0
W$^\pm$ ($W^\pm$)	80	$\pm$ 1	1
Z boson (Z)	91	0	1
Higgs boson (h)	125	0	0

TABLE 2. Bosons of the Standard Model [46].

interaction at low energies is $\alpha \approx 1/137$, at a momentum scale of 90 GeV it is $\alpha \approx 1/127$.

Weak Interaction

The weak interaction describes the interaction of fermions mediated by the neutral Z-boson and the charged W-bosons. Two fermions of the same type interact through the Z-boson. A lepton interacts within their same flavor neutrino through the W-boson. An up-type quark interacts with a down-type quark through the W-boson. The up-type quark interacts dominantly with a down-type quark from the same generation but generally the true eigenstates of the interaction is described by the Cabibbo-Kobayashi-Maskawa (CKM) matrix [46], seen in Figures 1 and 2. Owing to the small off-diagonal elements in the CKM matrix, B-hadrons have relatively long lifetimes of 1.5 ps. Secondary vertices are typically located approximately 1 mm from the interaction point.

Strong Interaction

The strong interaction describes the interaction of quarks and gluons mediated by the neutral massless gluon. The strong charge is referred to as color, there are three types and they are called red, green and blue. Quarks carry one color charge while gluons carry one color and one anti-color. The coupling constant α_s is approximately 0.12 at momentum scales around 90 GeV, and it increases at smaller momentum scales. At larger momentum scales, the coupling decreases leading to asymptotic freedom. Calculating the amplitude of high-energy hadron

collisions, such as proton-proton collisions, can be done by computing the integral

$$\sigma(pp \to X) = \sum_{ij} \int dx_1\, dx_2\, f_i(x)\, f_j(x)\, \hat{\sigma}(ij \to X)\,,$$

where $f_i(x)$ (known as Parton Distribution Functions [31]) describe the probability of the parton of flavor i to carry momentum fraction x of the hadron. Bottom quarks are produced in proton collisions and seen in ATLAS, when a bottom sea-quark from one proton gains a high transverse momentum from colliding with a gluon or quark in the other proton.

Higgs Mechanism

Massive weak bosons seemed to pose a problem with the local invariance of the electroweak Lagrangian. This is fixed by the Higgs mechanism [34, 37] in which the weak bosons end up with mass, while preserving the gauge invariance. A single complex scalar doublet field is introduced:

$$\Phi \equiv \begin{pmatrix} \phi^+ \\ \\ \phi^0 \end{pmatrix}\,.$$

along with a Higgs potential:

$$V(\Phi) = \mu^2\, \Phi^\dagger\, \Phi + \lambda\, \left|\Phi^\dagger\, \Phi\right|^2\,.$$

By requiring $\mu^2 < 0$ the minima of the Higgs potential is found to exist along

$$\Phi^\dagger\, \Phi = |\Phi|^2 = |\phi^+|^2 + |\phi^0|^2 = \frac{-\mu^2}{2\,\lambda}\,.$$

One can choose for the vacuum expectation value to be represented by

$$\langle \Phi \rangle = \begin{pmatrix} 0 \\ v/\sqrt{2} \end{pmatrix} ,$$

then excitations around the vacuum expectation can be represented by

$$\Phi(x) = \frac{1}{\sqrt{2}} \begin{pmatrix} 0 \\ v + h(x) \end{pmatrix} .$$

Expanding the kinetic term of the electroweak Lagrangian,

$$\frac{1}{8} \left| \begin{pmatrix} g_1 \, B_\mu + g_2 \, W_\mu^3 & g_2 \, (W_\mu^1 - i W_\mu^2) \\ g_2 \, (W_\mu^1 + i W_\mu^2) & g_1 \, B_\mu - g_2 \, W_\mu^3 \end{pmatrix} \begin{pmatrix} 0 \\ v \end{pmatrix} \right|^2 ,$$

and substituting

$$W_\mu^\pm \equiv \frac{1}{\sqrt{2}} (W_\mu^1 \mp i \, W_\mu^2) \, ,$$

and

$$Z_\mu \equiv \frac{1}{\sqrt{g_1^2 + g_2^2}} (g_2 \, W_\mu^2 - g_1 \, B_\mu) \, .$$

it becomes

$$\frac{1}{4} \, v^2 \, g_2^2 \, W_\mu^+ \, W^{-\mu} \frac{1}{4} \, v^2 \, (g_1^2 + g_2^2)^2 \, Z_\mu \, Z^\mu \, ,$$

giving rise to the boson masses

$$m_W = \frac{v \, g_2}{\sqrt{2}} \text{ and } m_Z = \frac{v}{\sqrt{2}} \sqrt{g_1^2 + g_2^2} \, .$$

Beyond The Standard Model

Dark Matter

Dark matter is matter which does not interact electromagnetically or strongly but does interact gravitationally. From astronomical observations such as the rotational speeds of galaxies it is known that dark matter accounts for 27% of the energy in the Universe [9, 50]. The SM has no particle which can fully account for dark matter and so it seems likely that there is some fairly stable weakly interacting and massive new particle. This would require an extension to the SM.

Fermion Mass Hierarchy Problem

The SM provides no explanation for the vast range of masses covered by the known fermions, from 1 eV for the neutrinos up to 173 GeV for the top quark. An extension to the SM with an extended Higgs sector can possibly explain this hierarchy[14].

Higgs Mass Hierarchy Problem

The electroweak scale, set by the Higgs, is around 100 GeV. Generally the Higgs mass receives large quantum corrections up to the Planck mass m_P, presumed to be around 10^{19} GeV. A Higgs mass that large would violate unitarity of WW and ZZ scattering [40]. Thus, the delicate cancellation required to keep the Higgs mass at the electroweak scale appears unnatural within the SM. Extensions to the SM, such as supersymmetry introduce new particles which naturally produce this cancellation, generally this is accompanied by an extended Higgs sector [45].

Two Higgs Doublet Model

Supersymmetric extensions to the SM generically require an extended Higgs sector to cancel gauge anomalies which would otherwise arise [45]. The simplest extension one can make is by requiring an additional complex scalar doublet field:

$$\Phi \equiv \begin{pmatrix} \phi_i^+ \\ \phi_i^0 \end{pmatrix},$$

where i=1,2. This results in 5 Higgs bosons, two neutral charge-parity (CP) even bosons, one neutral CP-odd Higgs boson and two charged Higgs bosons. The phenomenology of two Higgs doublet models is incredibly rich [17]. This analysis focuses on a model where one of the Higgses has small mass and has an enhanced coupling to down-type quarks with respect to the SM. The prospects for this search at the LHC appear to be good [16].

A General Extension to the SM

Generically, new Higgs bosons would have different couplings with respect to the SM Higgs, resulting in different process cross-sections. For example, in Type-2 2HDM, there can be an enhanced coupling between the CP-odd Higgs and down-type quarks. This is because the up-type quarks in a Type-2 2HDM couple to one Higgs doublet while the down-type couples to the other. Generically we will refer to the hypothetical new scalar as Φ. A previous search at LEP [8] resulted in limits on a model independent enhancement factor defined as

$$C^2_{b\bar{b}(\Phi\to\tau^+\tau^-)} \equiv \left(\frac{\lambda_{bb\Phi}}{\lambda_{bbh}}\right)^2 \times BR(\Phi \to \tau^+\tau^-),$$

where $\lambda_{bb\Phi}(\lambda_{bbh})$ is the BSM(SM) coupling for the Higgs to bottom-quarks and $BR(\Phi \rightarrow \tau^+\tau^-)$ is the BSM branching ratio of Higgs to di-tau. The LEP result covers a Φ mass range between 5 and 50 GeV and is shown in Figure 3.

$$\begin{pmatrix} d' \\ s' \\ b' \end{pmatrix} = \begin{pmatrix} V_{ud} & V_{us} & V_{ub} \\ V_{cd} & V_{cs} & V_{cb} \\ V_{td} & V_{ts} & V_{tb} \end{pmatrix} \begin{pmatrix} d \\ s \\ b \end{pmatrix}$$

FIGURE 1. The CKM matrix describing quark flavor mixing [46].

$$\begin{pmatrix} |V_{ud}| & |V_{us}| & |V_{ub}| \\ |V_{cd}| & |V_{cs}| & |V_{cb}| \\ |V_{td}| & |V_{ts}| & |V_{tb}| \end{pmatrix} \approx \begin{pmatrix} 0.97428 & 0.2253 & 0.00347 \\ 0.2252 & 0.97345 & 0.0410 \\ 0.00862 & 0.0403 & 0.99915 \end{pmatrix}$$

FIGURE 2. Magnitudes of CKM matrix [46].

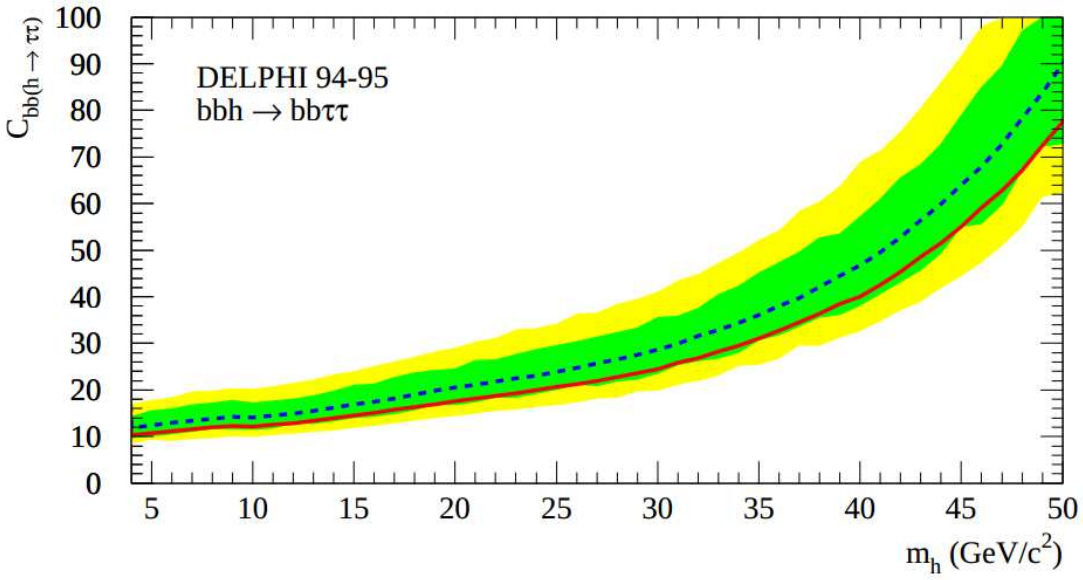

FIGURE 3. LEP limit result for model independent enhancement factor $C_{b\bar{b}(\Phi\to\tau^+\tau^-)}$ as function of Φ mass [8]. The dashed line and solid line show the median expected and observed exclusion limit. The green and yellow bands show the 1 and 2 standard deviation on the expected limit.

CHAPTER III

THE LHC AND ATLAS

The Large Hadron Collider

In 2012, the Large Hadron Collider [15] (LHC) collided protons at a center-of-mass energy ($\sqrt{s}$) of 8 TeV. This energy is achieved by ramping up energy in several accelerators. Collisions resulted in a peak instantaneous luminosity of $7{\times}10^{33}\mathtt{cm}^{-2}\mathtt{s}^{-1}$.

Protons are created using a duoplasmatron to ionize hydrogen gas. A series of accelerators are used to accelerate the protons: LINAC2 accelerates to 50 MeV, Proton Synchrotron accelerates to 25 GeV, and the Super Proton Synchrotron (SPS) accelerates to 450 GeV. After the SPS, protons enter the LHC. The LHC is 27 km in circumference and circulates proton beams using 1232 superconducting dipole magnets each with magnetic field strength exceeding 8 T. Quadrupole magnets focus the transverse beam size to an area of approximately 0.1 mm $\times$ 0.1 mm. A radio-frequency cavity system accelerates the beams up to the beam energy of 4 TeV per beam, within the LHC. The proton bunches are separated by as little as 50 ns. Before colliding, magnets squeeze the the beams to 16 μm in the transverse plane.

The ATLAS Detector

Overview

ATLAS [11, 5, 6] is located at Point 1 of the LHC tunnel. Layers of detectors are used to detect different types of interactions and create an image of interesting

proton collisions. Moving from the center of the detector outwards[1], the detector is made up of the inner detector, electromagnetic and hadronic calorimeters, and the muon spectrometer. Spaced within the detector components are the superconducting magnet systems which bend charged particle trajectories allowing for momentum measurement. A substantial computational component is necessary to sift through the enormous flow of data.

Inner Detector

The inner detector is responsible for tracking of charged particles at a high precision. Three subsystems make up the inner detector and cover up to a pseudorapidity of $|\eta|$ <2.5. The inner-most Pixel detector is enclosed by the Semi-Conductor Tracker (SCT) which is surrounded by the Transition Radiation Detector (TRT).

During 2012, the Pixel detector had three layers of fine granularity silicon detectors, containing 80 M channels. The first layer (B-layer) starts 5 cm from the beam axis and provides secondary vertex information necessary for identifying bottom-quark jets, for example. The pixel size is 50 μm in $R-\phi$ by 400 μm in z.

The SCT is made of silicon detector strips with a slightly poorer resolution than the Pixel detector. The strip size is 17 μm in $R-\phi$ by 580 μm in z.

The TRT relies on radiation from relativistic, charged particles transitioning between mediums with different dielectric constants. It is made up of 4 mm

[1]ATLAS uses a right-handed coordinate system [16]. The x-axis points to the center of the LHC ring. The y-axis points upwards. The z-axis points along the beam line. The spherical coordinates ϕ and θ are defined as follows. The azimuthal angle, ϕ, measures the angle in the xy-plane beginning along the positive x-axis and increases towards the positive y-axis. The angle measured from the positive z-axis, θ, is specified by the pseudorapidity, η, and is defined as $\eta = -\ln(\tan\frac{\theta}{2})$. The transverse momentum, p_T, is defined in the x-y plane. The distance ΔR in the η-ϕ space is defined as $\Delta R = \sqrt{\Delta\eta^2 + \Delta\phi^2}$.

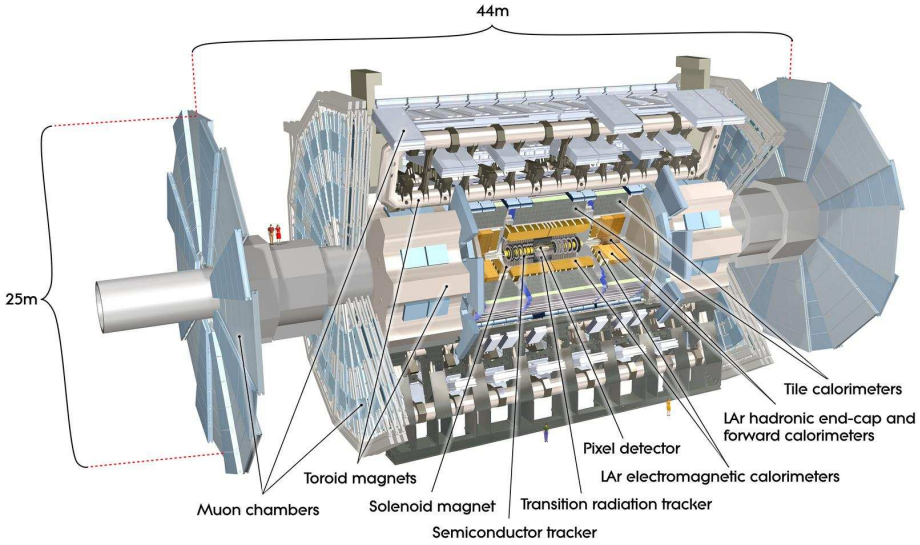

FIGURE 4. An illustration of the ATLAS detector [5].

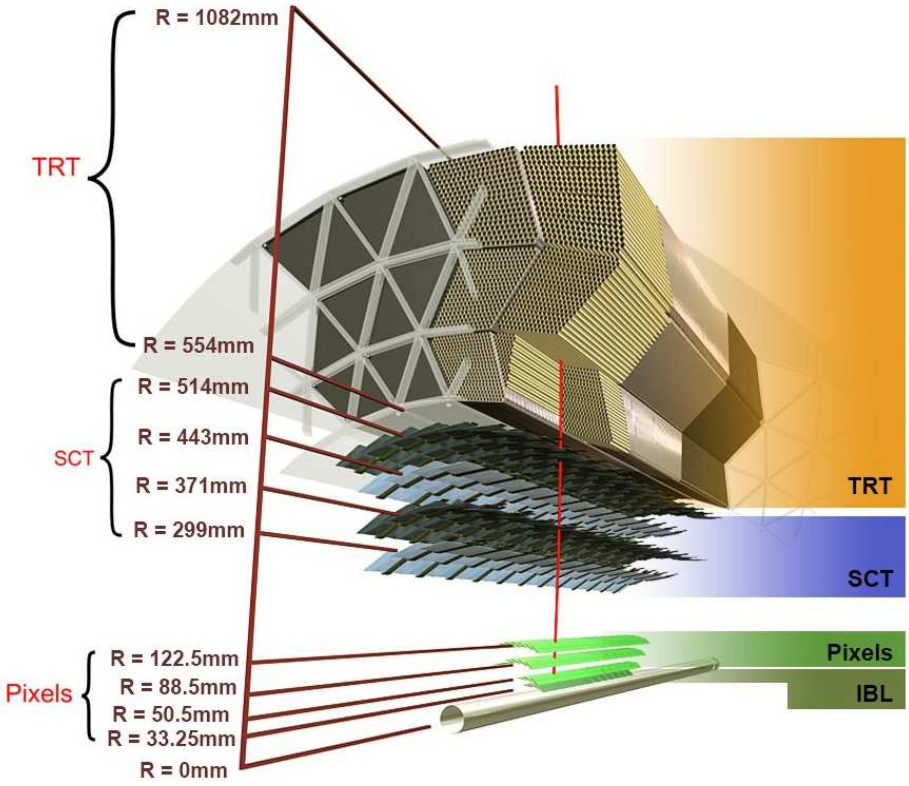

FIGURE 5. An illustration of the inner detector of ATLAS [5].

diameter straws filled with ionizing gas which serves to detect charged particles. Two thresholds are used, low threshold provides for general tracking while a high threshold discriminates transition radiation [30]. The TRT has poorer resolution still compared to the SCT, however a high number of hits is expected. The TRT has 420000 channels and covers up to a pseudorapidity of $|\eta| < 2.0$.

Calorimeters

The ATLAS calorimeter is used to measure energy deposits of high energy electrons, photons, and hadrons. It is made up of the electromagnetic and hadronic calorimeters. Each is constructed with alternating layers of dense absorber material and an active detecting material.

There are several parts to the electromagnetic calorimeter, the barrel, the presampler and the end-caps. At the interface of the barrel and end-cap portions ($|\eta| \approx 1.47$) a small gap exists for cabling, the energy reconstruction for particles passing through this crack is poor. The end-caps covers up to $|\eta| < 2.5$ so the electromagnetic calorimeter provides full coverage of the inner detector. The presampler covers $|\eta| < 1.8$ corrects for energy losses due to dead material in front of the calorimeter. The absorber material is lead, while the detecting material is liquid argon with copper-tungsten electrodes.

Two components make up the hadronic calorimeter, the tile covers $|\eta| < 1.7$ while the hadronic end-cap covers up to $|\eta| = 3.2$. The tile calorimeter uses steel absorber and scintillating tiles as the detecting material. The hadronic end-cap uses copper absorbers and liquid argon detecting material. The forward calorimeter covers approximately $3.1 < |\eta| < 4.9$ and uses liquid argon detecting material with copper and tungsten absorbing material.

Muon Spectrometer

The muon spectrometer is used to measure muon tracks with monitored drift tubes (MDT), cathode strip chambers (CSC), resistive plate chambers (RPC) and thin gap chambers (TGC). There are three layers of monitored drift tubes containing 93% argon and 7% CO_2. They cover a range of $|\eta|$ <2.7 except for the inner most layer which covers $|\eta|$ <2.0. The region 2.0< $|\eta|$ <2.7 in the inner layer is covered by the CSC. The trigger system covers a range of $|\eta|$ <2.4 and uses the resistive plate chambers in the barrel and thin gap chambers in the end-cap.

Magnet Systems

The magnet systems of ATLAS bend traveling charged particles inversely proportional to their momentum. An accurate map of the magnetic field strength coupled with track information resolves momentum of these charged particles.

The central solenoid is responsible for bending particles within the inner detector, with a field strength of 2 T along the beam axis. The solenoid has a length of 5.8 m and diameter of 2.5 m.

The toroid is responsible for bending muons traveling through the muon spectrometer. It covers a volume from 5 to 20 m in diameter and 26 m in length. The toroid is divided into a barrel and end-cap region, the barrel region covers $|\eta|$ <1.4 while the end-cap region covers 1.6< $|\eta|$ <2.7. Each section is made up of 8 independent coils producing peak magnetic field strengths of 4 T. The toroidal shape creates fields bending muons in η.

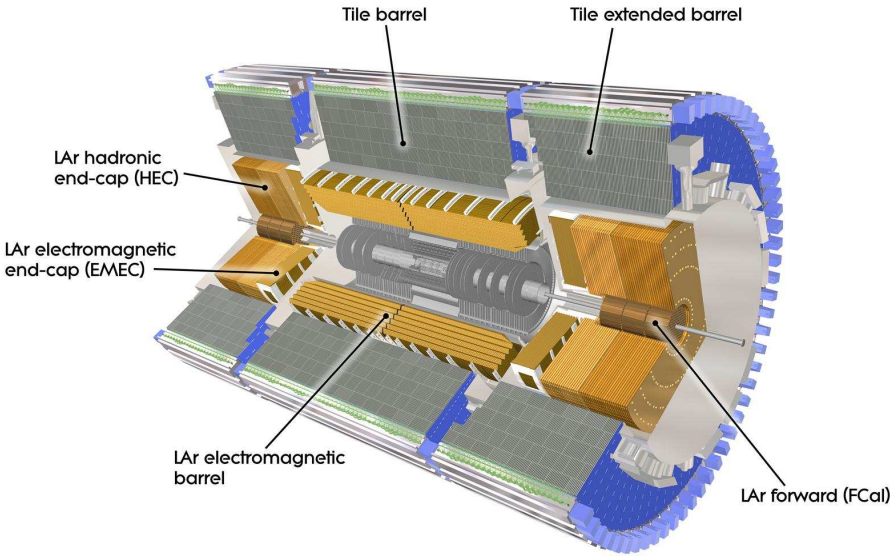

FIGURE 6. An illustration of the calorimeters of ATLAS [5].

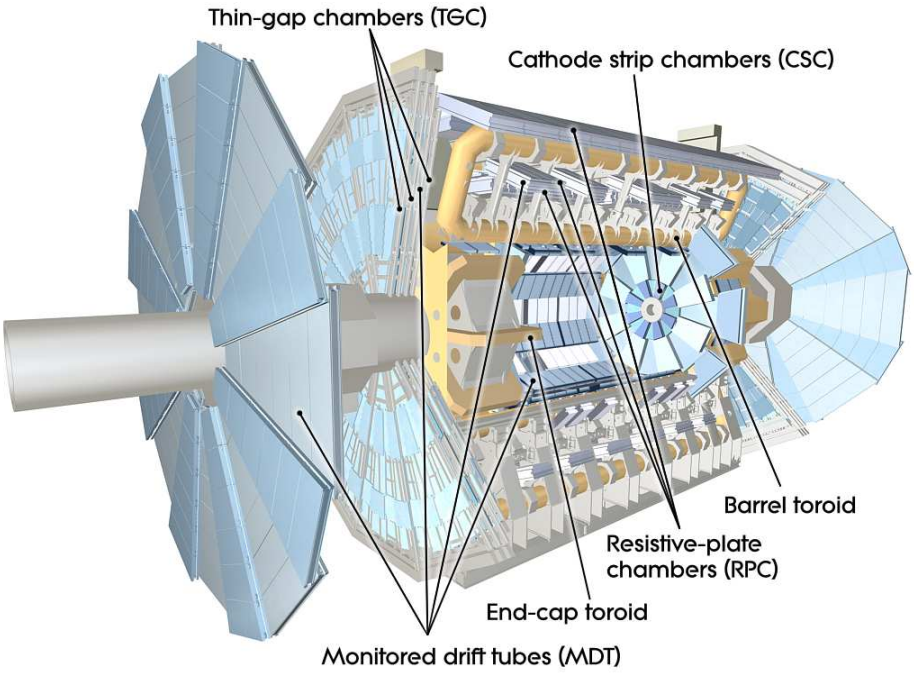

FIGURE 7. An illustration of the muon system of ATLAS [5].

ATLAS Detector Response

Pileup

Due to the high instantaneous luminosity at the LHC, several distinct collisions can occur in the same bunch crossing. Overlap of particles produced from different beam particle interactions in the same bunch is known as in-time pileup. Another similar issue, caused by the finite detector response speed, results in the overlap of electronic signals. This is known as out-of-time pileup. The tracking algorithms, for the 2012 data, were constructed such that their response is largely independent of the in-time pileup value. In 2012 running, the mean number of interactions per bunch crossing (μ) averaged about 20.

Trigger

In the 2012 run, the ATLAS trigger system employed three levels to reduce the collision data rate to a level that can be saved and used in analysis. The first level (L1) relied on custom hardware while the second (L2) and third Event Filter (EF) levels relied on software running on CPU farms [5].

Level 1

The L1 trigger reduces the bunch-crossing rate of 20 MHz to about 65 kHz. Triggers are created using course information from the calorimeters and muon system. After a L1 accept, regions of interest (RoIs) are passed to L2.

For this analysis, which requires one electron and one muon, a combined muon-electron trigger was used to collect data. A second sample discussed in chapter 4.4, required two muons and relied on a di-muon trigger to collect data.

The low-transverse-momentum muon trigger, used in the combined muon-electron trigger, required 2(3) layers of coincidence in the barrel(end-cap) region of the muon spectrometer. The high-transverse-momentum muon trigger, used in the the di-muon trigger, required 3 layers of coincidence [28]. The electron portion of the trigger in the muon-electron trigger are based on 0.1×0.1 towers in the calorimeters. This particular trigger required less than 1 GeV of energy deposited in the hadronic calorimeter.

Level 2

The L2 trigger reduces the event rate to about 6.5 kHz. Full granularity information is retrieved for RoIs provided by L1. After a L2 accept, the Event Builder (EB) builds events using the entire scope of the detector which is passed to the EF.

Event Filter

The EF trigger reduces the event rate to about 500 Hz. Events are triggered based on detailed object identification and event characteristics. Events selected by the EF are subsequently stored indefinitely for use in analysis. Events are sorted into "streams" according to their trigger, for instance events that triggered electron or photon triggers will be stored in the `Egamma`[2] stream. Events which triggered muon triggers will be stored in the `Muons` stream.

For this analysis the electron-muon trigger requires a transverse momentum of 12 GeV for the electron and 8 GeV for the muon. The plateau efficiency for the muon portion is approximately 80% [28] while for the electron portion it is

[2]This `font style` indicates specific meaning in ATLAS analysis

approximately 100% [48]. The di-muon trigger requires a transverse momentum of 18 GeV for the leading muon and 8 GeV for the subleading muon.

Event Reconstruction

Reconstruction algorithms find objects and event properties, such as muons or electrons. The Athena framework of ATLAS [33] contains these algorithms and is used to generate analysis level data formats with collections of identified objects and calculated event properties. An analysis selects for events matching a certain set of criteria, in the case of this thesis, the analysis is designed to select a region where a new physics signal could be observed.

Tracking

Hits produced in the inner-detector are used to construct charged particle tracks. Space points beginning in the Pixel detector are added to by the SCT detectors and construct segments of a track. The track segment is extrapolated outwards to find hits in the TRT. Space points update the track parameters with a Kalman filter [39]. Outside-in tracking begins in the TRT detector constructing track segments from remaining TRT hits and then extrapolates backwards into the Pixel and SCT detectors.

Track parameters computed in this procedure are as follows:

- d_0: The transverse impact parameter, the closest distance to the interaction point in the xy-plane
- z_0: The longitudinal impact parameter, the closest distance to the interaction point in the z-plane

– ϕ_0: The azimuthal angle at the point of the interaction

– θ: The polar angle

– $\frac{q}{|p|}$: The ratio of charge to absolute momentum

Clustering

Energy, from the electromagnetic and hadronic calorimeters, is clustered together topologically [42]. Cells which rise above 4 times the absolute value of the noise level are used to seed these clusters. Cells bordering the seed are added to the cluster if they are above 2 times the absolute value of the noise level.

Topological clusters are used in reconstruction of jets using the anti-k_t algorithm [20]. The anti-k_t algorithm is discussed in section 3.3.

Muons

Muons are reconstructed by matching track segments from the muon spectrometer to tracks in the inner detector. The efficiency of reconstructed muons is greater than 95% for $|\eta| > 0.1$ [27].

Electrons

Clusters of high energy in the electromagnetic calorimeter are used to seed the sliding window algorithm which in turn seeds the electron reconstruction algorithm. Tracks from the inner detector are matched to the calorimeter seed. Further quality requirements reduce electrons fakes from pions. The requirements include cuts on the shape of the electron's shower in the electromagnetic calorimeter, tight tracking requirements and matching of tracks to clusters, and

high-threshold hits in the TRT. This analysis uses the medium selection criteria which is approximately 90% efficient [4].

Jets

In a hard scattering event, a quark or gluon (partons) can be ejected from either proton. The color is immediately neutralized due to the properties of confinement of the strong force. This results in hadronization which looks like a spray of energy in the calorimeters. The goal of jet reconstruction is to estimate the parton kinematics from these calorimeter energy deposits.

Jets in this analysis are reconstructed with the anti-k$_t$ algorithm [20], using the distance parameter R=0.4, and taking topological clusters as inputs. To calibrate the energy, a local cell signal weighting (LCW) method is used [26].

Pileup can produce jets that typically have tracks associated with a vertex different from the primary vertex. Tracks are associated with a jet, if the jet axis aligns with the extrapolated track axis within $\Delta R < 0.4$. A discriminant called the jet vertex fraction (JVF) is defined as the ratio of the sum of tracks' transverse momentum associated to the primary vertex to all tracks. The JVF is used to discriminate jets from the hard scattering event from pileup jets. Pileup jets will tend to value of 0 while hard scattering jets will tend to a value of 1. This analysis requires a JVF of greater than 50% for jets with transverse momentum less than 50 GeV.

Simulation

Monte Carlo event samples are necessary to estimate certain background processes. Monte Carlo samples used in this analysis were produced in the MC12a ATLAS campaign.

Monte Carlo Event Generation

Monte Carlo (MC) matrix element generators are used to generate proton-proton scattering events. The specific generators used for signal and background processes are discussed in Chapter 4.2.

Detector Simulation

Events from the generation step are processed with GEANT4 [10] to model the ATLAS detector response. Minimum bias pileup events generated with PYTHIA [51] are overlaid onto the event. Digitization algorithms simulate the sub-detector response of the event and output data formatted as if it were coming from the ATLAS detector. From this point onward, the events are treated by the same algorithms as used on real ATLAS data.

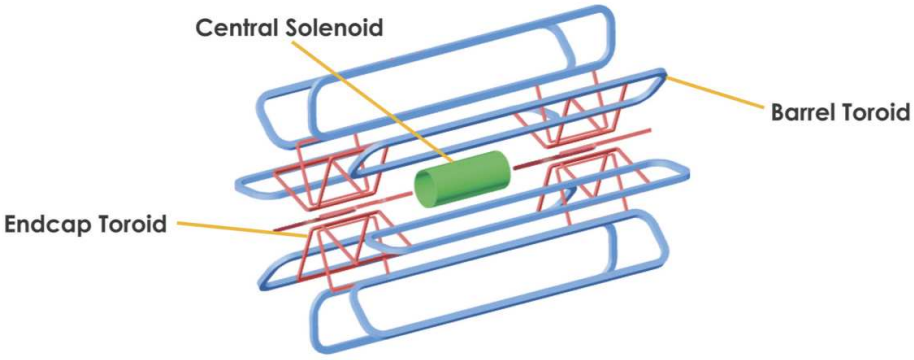

FIGURE 8. An illustration of the magnet systems of ATLAS [47].

CHAPTER IV

SEARCH FOR LOW-MASS $\Phi \to \tau_e\tau_\mu$ PRODUCED IN ASSOCIATION WITH A BOTTOM-JET

Introduction

This analysis searches for new scalar bosons produced in association with a bottom-quark and decaying to two tau leptons, resulting in a final state of an electron, muon, bottom-jet and missing energy. The ATLAS data samples are discussed followed by the object selection. The SM background estimation is discussed including data-driven backgrounds for QCD Multi-jet and $Z/\gamma^* \to \tau_e\tau_\mu$ + jets SM backgrounds. Several event selections are outlined including validation regions and the final signal selection region. The various systematic uncertainties are discussed and finally the result is presented.

Data Samples

Data

In 2012, with the LHC colliding proton bunches at $\sqrt{s} = 8$ TeV, ATLAS recorded the 20.3 fb^{-1} of integrated luminosity used by this analysis. The events used in this analysis were collected from the `Egamma` data stream requiring each event pass the electron-muon trigger `EF_e12Tvh_medium1_mu8`. Events used for the embedded sample discussed in Chapter 4.4 were collected from the `Muon` data stream requiring each event pass the di-muon trigger `EF_mu18_tight_mu8_EFFS`.

Simulation

Signal and background processes were modeled by Monte Carlo (MC) simulation. Simulated events are reweighted to reproduce the distribution of number of primary vertices per bunch crossing seen in data. Corrections to simulated events are made for object reconstruction and identification, these are discussed per object.

The signal process $b\Phi(\Phi \rightarrow \tau^+\tau^-) + jets$ was simulated using SHERPA [35] and includes up to five associated light jets. Events are preselected to include one electron, muon and bottom-jet with requirements on the transverse momentum and pseudorapidity, as shown in Table 3. Signal is normalized to cross-sections calculated with MCFM [21] and with fiducial requirements made by RIVET [18]. The fiducial cross-section includes the tau lepton branching ratio but assumes 100% branching fraction of $\Phi \rightarrow \tau^+\tau^-$ which is in alignment with the definition of $C_{b\bar{b}(\Phi\rightarrow\tau^+\tau^-)}$ from Chapter 2.3.

The processes W and Z/γ^* produced in association with jets were simulated using ALPGEN [44]. The $t\bar{t}$ process was simulated using POWHEG [12]. The diboson processes were simulated using HERWIG [32]. Simulated processes use the CT10 parton distribution functions [41]. Except for SHERPA simulated processes, additional libraries are used for modelling tau decay and photons radiated by charged leptons. TAUOLA [38] is used to model tau decays. PHOTOS [13] is used to model additional photon radiation from charged leptons.

TABLE 3. Requirements defining fiducial signal region.

muon	$p_T > 8$ GeV	$\|\eta\| < 3.0$
electron	$p_T > 12$ GeV	$\|\eta\| < 3.0$
bottom-jet	$p_T > 15$ GeV	$\|\eta\| < 3.0$

The cross-sections used to normalize simulated signals and backgrounds are summarized in Table 4.

Object Selection

Object selections are summarized here and are based on information discussed in Chapter III.

Muons

Muons recontructed by the STACO [29] algorithm and passing the tight STACO Combined quality requirement are used in this analysis. Muons are required to have transverse momentum $p_T > 10$ GeV and with pseudorapidty $|\eta| < 2.5$. To remove cosmic muons, the muon track extrapolated to the beam line must be within 10 mm of the primary vertex. The ATLAS Muon Combined Performance Group recommends additional quality requirements to reduce fake rates from displaced hadrons. A summary of the object requirements can be found in Table 5.

TABLE 4. Cross-sections for simulated samples

Process	Cross-section (pb)
$W \to l + jets$ $(l = e, \mu, \tau)$	12.22×10^3
$Z/\gamma^* \to ll + jets(m_{ll} > 60GeV)$	1.15×10^3
$t\bar{t}$	137.3
Diboson WW, WZ and ZZ	20.6, 6.8, 1.55
Signal Process $C_{b\bar{b}(\Phi\to\tau^+\tau^-)} = 5$	Cross-section (pb)
$b\Phi(M_\Phi$=20 GeV)	0.278
$b\Phi(M_\Phi$=30 GeV)	0.235
$b\Phi(M_\Phi$=50 GeV)	0.180
$b\Phi(M_\Phi$=70 GeV)	0.176

TABLE 5. A summary of muon requirements. SCT and TRT refer to those detectors dicussed in Chapter 3.3.

Muons
$p_T > 10$ GeV
$\|\eta\| < 2.5$
`staco_tight`
Require a B-layer hit if expected
$N(\text{pixel hits}) + N(\text{pixel dead}) \geq 2$
$N(\text{SCT hits}) + N(\text{SCT dead}) \geq 6$
$N(\text{pixel holes}) + N(\text{SCT holes}) \leq 2$
if $\|\eta\| < 1.9$:
$N(\text{TRT Outliers}) < 0.9 \times (N(\text{TRT Hits}) + N(\text{TRT Outliers}))$ and
$(N(\text{TRT Hits}) + N(\text{TRT Outliers})) > 5$
elif $(N(\text{TRT Hits}) + N(\text{TRT Outliers})) > 5$:
$N(\text{TRT Outliers}) < 0.9 \times (N(\text{TRT Hits}) + N(\text{TRT Outliers}))$

TABLE 6. A summary of electron requirements.

Electrons
$p_T > 15$ GeV
$\|\eta\| < 2.47$ and not in $1.37 < \|\eta\| < 1.52$
`mediumPP`
non-overlapping with muon

TABLE 7. Summary of jet requirements.

Jets
$p_T > 20$ GeV
$\|\eta\| < 2.4$
JVF $> 50\%$
non-overlapping with muon or electron

The Muon Combined Performance Group provides muon momentum scale and resolution corrections for MC simulation as well as muon identification efficiency corrections [2].

To reduce events with muons produced in jets, muons are defined to be `isolated` or `partially isolated` according to:

$$\texttt{isolated}: \begin{cases} \texttt{etcone20}/p_T < 5\% \texttt{ and} \\ \texttt{ptcone40}/p_T < 8\% \end{cases}$$

$$\texttt{partially isolated}: \begin{cases} 5\% < \texttt{etcone20}/p_T < 10\% \texttt{ or} \\ 8\% < \texttt{ptcone40}/p_T < 16\% \end{cases}$$

where `etcone20` is defined as the sum of transverse energy of calorimeter cells within $\Delta R < 0.2$ of the muon. The `ptcone40` variable is defined as the sum of the p_T of tracks with $p_T > 1$ GeV and within $\Delta R < 0.4$ of the muon.

Electrons

Electrons passing the `Medium++` of the standard electron identification algorithms [4] are used in this analysis. Electrons are required to have transverse energy $E_T > 15$ GeV and within a pseudorapidity $|\eta| < 2.47$ and excluding the transition region between the barrel and end-cap calorimeters $1.37 < |\eta| < 1.52$. A summary of the object requirements can be found in Table 6.

The EGamma Performance Group provides electron energy scale and resolution corrections for MC simulation as well as electron identification efficiency corrections [25, 4].

The electrons use the same definitions of `isolated` and `partially isolated` as are defined for muons. If a selected electron overlaps within ΔR < 0.2 of a muon it is removed from the event.

Jets

The jets used in this analysis are reconstructed with the anti-k_t algorithm [20] with radius $R = 0.4$ and using topological clusters [42] as inputs. The jets are calibrated using the local cell signal weighting (LCW) method [26]. Jets are required to have transverse momentum $p_T > 25$ GeV and be within a pseudorapidity $|\eta| < 2.4$. To reduce the effect of pileup, jets with $p_T < 50$ GeV are required to have a jet vertex fraction (JVF) greater than 50%. A summary of the object requirements can be found in Table 7.

The MV1 bottom-tagging algorithm [1] is used to tag jets as likely bottom-jets. The working point used in this analysis corresponds to a bottom-tagging efficiency of 70% in $t\bar{t}$ samples. Corrections to bottom-tagging efficiency [3] are made for simulated samples.

If a jet overlaps within ΔR < 0.2 of a muon or electron it is removed from the event.

Event Characteristics

Several other definitions are necessary for this analysis. The sum transverse energy of the event is defined as

$$\sum E_{\mathrm{T}} \equiv \sum_{\text{particles}} E_{\mathrm{T}}^{\text{particle}}$$

where $E_{\mathrm{T}}^{\mathrm{particle}}$ is the transverse energy of the particle. Leptons and jets are included in the sum. The missing energy vector is defined as

$$\vec{E}_{\mathrm{T}}^{\mathrm{miss}} \equiv - \sum_{\mathrm{particles}} \vec{E}_{\mathrm{T}}^{\mathrm{particle}}$$

where $\vec{E}_{\mathrm{T}}^{\mathrm{particle}}$ is the transverse energy vector of the particle. Leptons and jets are included in the sum. The transverse mass of particle and missing energy is defined as

$$M_{\mathrm{T}}(\vec{E}_{\mathrm{T}}^{\mathrm{miss}}, \mathrm{particle}) \equiv \sqrt{E_{\mathrm{T}}^{\mathrm{miss}} E_{\mathrm{T}}^{\mathrm{particle}} \times (1 - cos(\phi^{\mathrm{miss}} - \phi^{\mathrm{particle}}))}$$

The jet energy H_{T} is the sum transverse energy of the event where only jets are included in the sum.

Background Estimation

Several important backgrounds are estimated. The $t\bar{t}$, W+jets and diboson processes are estimated from MC simulation. The $Z \rightarrow \tau_e\tau_\mu$ and QCD multi-jet processes use data-driven techniques discussed below to estimate their contribution to the signal region.

Embedded $Z \rightarrow \mu\mu$ + jets

$Z/\gamma^* \rightarrow \tau_e\tau_\mu$ events are an irreducible background for a low-mass $\Phi \rightarrow \tau_e\tau_\mu$ signal. $Z/\gamma^* \rightarrow \mu^+\mu^-$ events are uncontaminated by $\Phi \rightarrow \mu^+\mu^-$ signal because of the expected low coupling of Φ to the light $\mu^+\mu^-$. The topology of $Z/\gamma^* \rightarrow \mu^+\mu^-$ and $Z/\gamma^* \rightarrow \tau^+\tau^-$ events are the same when the difference in mass between taus and muons are taken into account. A clean sample of $Z/\gamma^* \rightarrow \mu^+\mu^-$ can be found in data by making the basic selection described in 4.5, see figure 9. In

this sample, muons are replaced tau leptons, whose decay is simulated using the TAUOLA software package. The resulting sample is then reweighted according to the differences observed when applying this procedure to simulated $Z/\gamma^* \rightarrow \mu^+\mu^-$ and comparing to simulated $Z/\gamma^* \rightarrow \tau^+\tau^-$. The sample is reweighted as a function of the electron and muon p_T as well as the electron η. By applying this full embedding and reweighting procedure to simulated $Z/\gamma^* \rightarrow \mu^+\mu^-$ the procedure is validated to not produce biases in the distributions which have not been explicitly reweighted, see Figure 10. The weights determined from the basic selection are applied to all other selections. Different weight tables are determined for use in other control region when leptons are required to be partially isolated. Different weight tables are generated corresponding to the various lepton systematic uncertainties.

QCD Multi-jet

The QCD multi-jet background produces electrons and muons from bottom decay. These leptons are typically non-isolated but due to the huge cross-section of this background, a significant number of events appear in our signal selection. Also, owing to the large cross-section of this background, a sufficient sample cannot be simulated in order to estimate its contribution to the total background. The "*ABCD method*" [43] is employed in order to estimate the background. The multi-jet background is very symmetric in events with leptons of opposite-sign (OS) and same-sign (SS). The OS/SS ratio computed from events with non-isolated leptons can be used to reweight events with SS and isolated leptons to determine the contribution of QCD multi-jet in a selection of events with OS and isolated leptons. Therefore four regions are defined:

– A: Signal region with isolated opposite-sign leptons

– B: Control region with isolated same-sign leptons

– C: Signal region with a non-isolated muon and opposite-sign electron

– D: Signal region with a non-isolated muon same-sign electron

In the control regions {B, C, D}, known backgrounds are subtracted from data and bin-by-bin the following formula is used to estimate QCD Multi-jet in signal region A:

$$N^{\mathrm{A}}_{\mathrm{Multi-jet}} = N^{\mathrm{B}}_{\mathrm{Multi-jet}} \times \frac{N^{\mathrm{C}}_{\mathrm{Multi-jet}}}{N^{\mathrm{D}}_{\mathrm{Multi-jet}}}\,.$$

Validation of this method is found in Chapter 4.5.

Event Selection

Several selections are used to validate background estimation. These selections are defined to isolate the particular background in order to check for correctness of overall normalization as well as shape of various distributions. The signal selection is defined to reduce background processes, while maintaining a high efficiency for signal processes.

Basic Selection

The basic selection requires exactly one isolated electron, one isolated muon and at least one jet, all satisfying the requirements outlined in Chapter 4.3. Events are required to satisfy the electron-muon trigger `EF_e12Tvh_medium1_mu8`. The invariant mass of the electron and muon is required to be less than 100 GeV. The sum E_{T} must be less than 300 GeV while $M_{\mathrm{T}}(\vec{E}^{\mathrm{miss}}_{\mathrm{T}}, \mathrm{muon}) + M_{\mathrm{T}}(\vec{E}^{\mathrm{miss}}_{\mathrm{T}}, \mathrm{electron})$

must be less than 160 GeV. The isolation requirement reduces QCD multi-jet to manageable levels. The invariant mass requirement restricts the events to our scope of interest. The energy requirements reduce $t\bar{t}$ and W+jets significantly.

The basic selection for embedding makes the same requirements as above, except the electron is replaced with a muon with $p_T > 20$ GeV and the required di-muon trigger `EF_mu18_tight_mu8_EFFS` replaces the electron-muon trigger.

Event counts following the basic selection can be found in Table 8. A variety of distributions for events satisfying the basic selection are shown in Figures 11, 12 and 13.

Subsequent selections make tighter requirements in the sum $E_{\mathrm{T}} \times M_{\mathrm{T}}(\vec{E}_{\mathrm{T}}^{\mathrm{miss}}, \mathrm{muon}) + M_{\mathrm{T}}(\vec{E}_{\mathrm{T}}^{\mathrm{miss}}, \mathrm{electron})$ plane. The two-dimensional event counts for a select signal sample and $t\bar{t}$ and W + jets backgrounds is shown in Figure 14.

Z+jets Validation

The Z+jets validation selection makes all the same requirements as the basic selection. Additionally, the sum E_{T} must be less than 200 GeV while $M_{\mathrm{T}}(\vec{E}_{\mathrm{T}}^{\mathrm{miss}}, \mathrm{muon}) + M_{\mathrm{T}}(\vec{E}_{\mathrm{T}}^{\mathrm{miss}}, \mathrm{electron})$ must be less than 80 GeV. A minimum sum jet energy H_{T} of 30 GeV is required. The sum E_{T} and sum M_{T} energy

Sample	Counts
Z/γ^* + jets	19542.5 ± 29.36
QCD Multi-jet	5979.63 ± 113.4
$t\bar{t}$	10010.62 ± 71.93
W + jets	1005.36 ± 68.29
Diboson	1542.06 ± 23.46
total SM	38080.18 ± 155.27
data	37171.0

TABLE 8. Event counts after basic selection. Backgrounds in red are estimated using data-driven techniques.

requirements reduce $t\bar{t}$ and W+jets further. The jet energy requirement reduces QCD multi-jet. This selection is similar to the final signal, but it does not require a bottom-tagged jet.

Event counts following the Z+jets validation selection can be found in Table 9. A variety of distributions for events satisfying the Z+jets validation selection are shown in Figures 15, 16 and 17.

$t\bar{t}$ Validation

The $t\bar{t}$ validation selection makes all the same requirements as the basic selection. Additionally, the sum E_{T} must be greater than 200 GeV while $M_{\mathrm{T}}(\vec{E}_{\mathrm{T}}^{\mathrm{miss}}, \mathrm{muon})$+$M_{\mathrm{T}}(\vec{E}_{\mathrm{T}}^{\mathrm{miss}}, \mathrm{electron})$ must be greater than 80 GeV. Finally, at least one jet in the event must satisfy the bottom-tagging criteria. These requirements create a very pure $t\bar{t}$ sample with which to validate our normalization.

Event counts following the $t\bar{t}$ validation selection can be found in Table 10. A variety of distributions for events satisfying the $t\bar{t}$ validation selection are shown in Figures 18, 19 and 20.

Sample	Counts
$b\Phi(M_{\Phi}$=30 GeV)	440.25 ± 19.11
Z/γ^* + jets	9940.14 ± 20.89
QCD Multi-jet	2747.32 ± 63.26
$t\bar{t}$	1548.18 ± 28.42
W + jets	217.2 ± 23.65
Diboson	279.32 ± 9.8
total SM	14732.16 ± 76.82
data	14483.0

TABLE 9. Event counts after Z+jets validation selection. Backgrounds in red are estimated using data-driven techniques. Signal assumes $C_{b\bar{b}\Phi} = 5$.

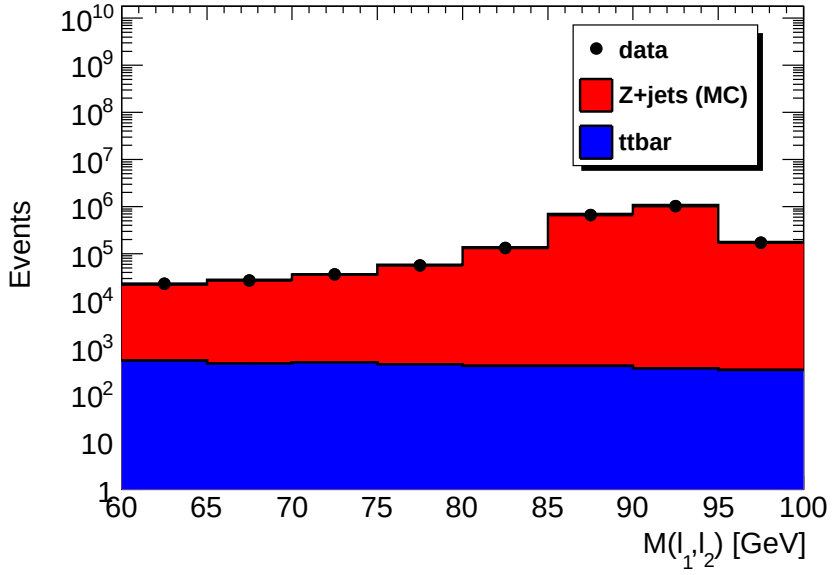

FIGURE 9. Di-muon invariant mass distribution after basic selection.

Sample	Counts
Z/γ^* + jets	54.96 ± 1.63
$t\bar{t}$	3477.45 ± 41.64
W + jets	4.83 ± 2.56
Diboson	9.63 ± 1.92
total SM	3546.86 ± 41.8
data	3413.0

TABLE 10. Event counts after $t\bar{t}$ validation selection. Backgrounds in red are estimated using data-driven techniques.

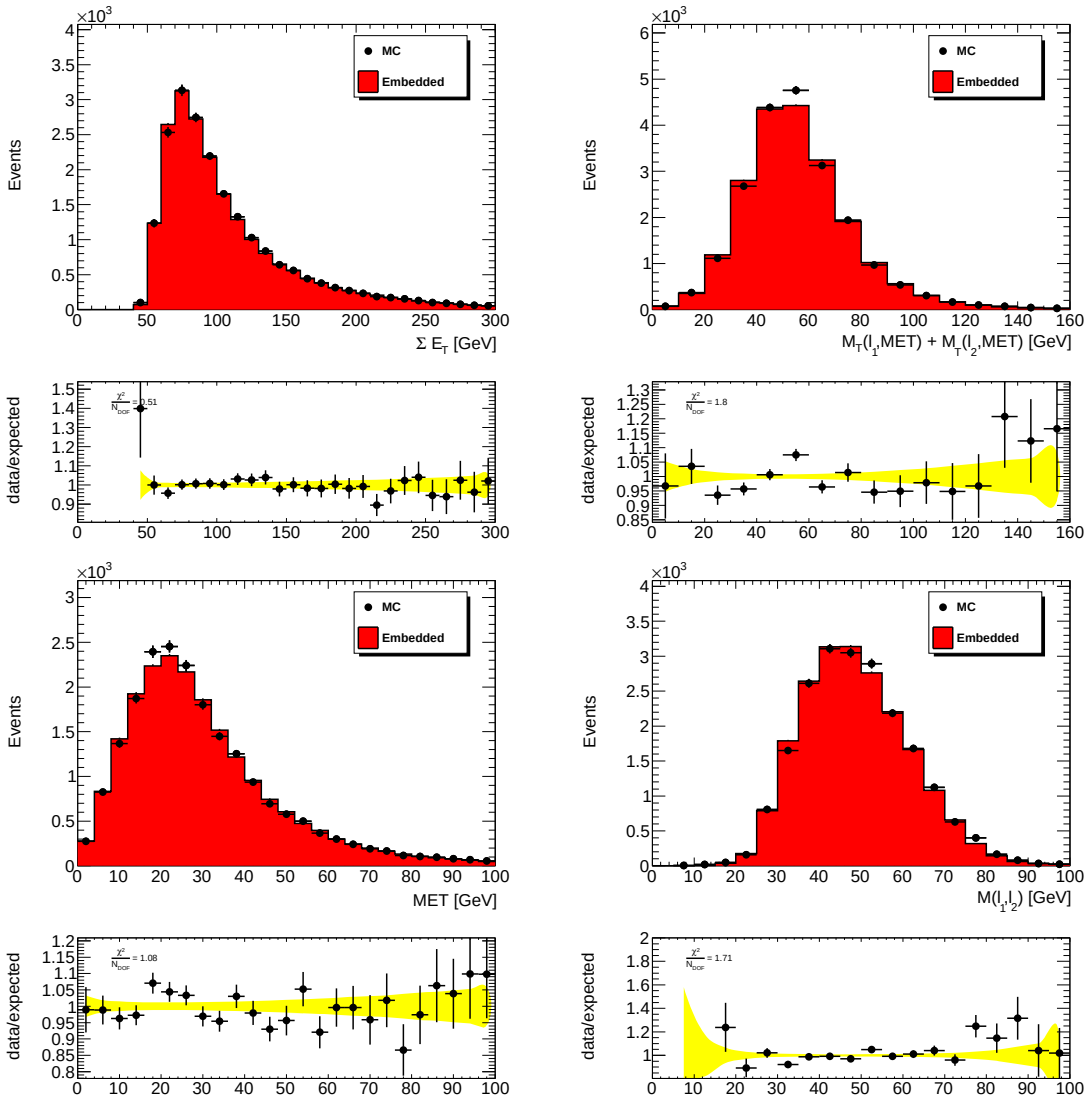

FIGURE 10. Event kinematics after basic selection, comparing embedded simulation $Z/\gamma^* \rightarrow \mu^+\mu^-$ to simulation $Z/\gamma^* \rightarrow \tau^+\tau^-$. (Top) Scalar sum of transverse energy, sum of transverse mass. (Bottom) Missing transverse energy, lepton pair invariant mass.

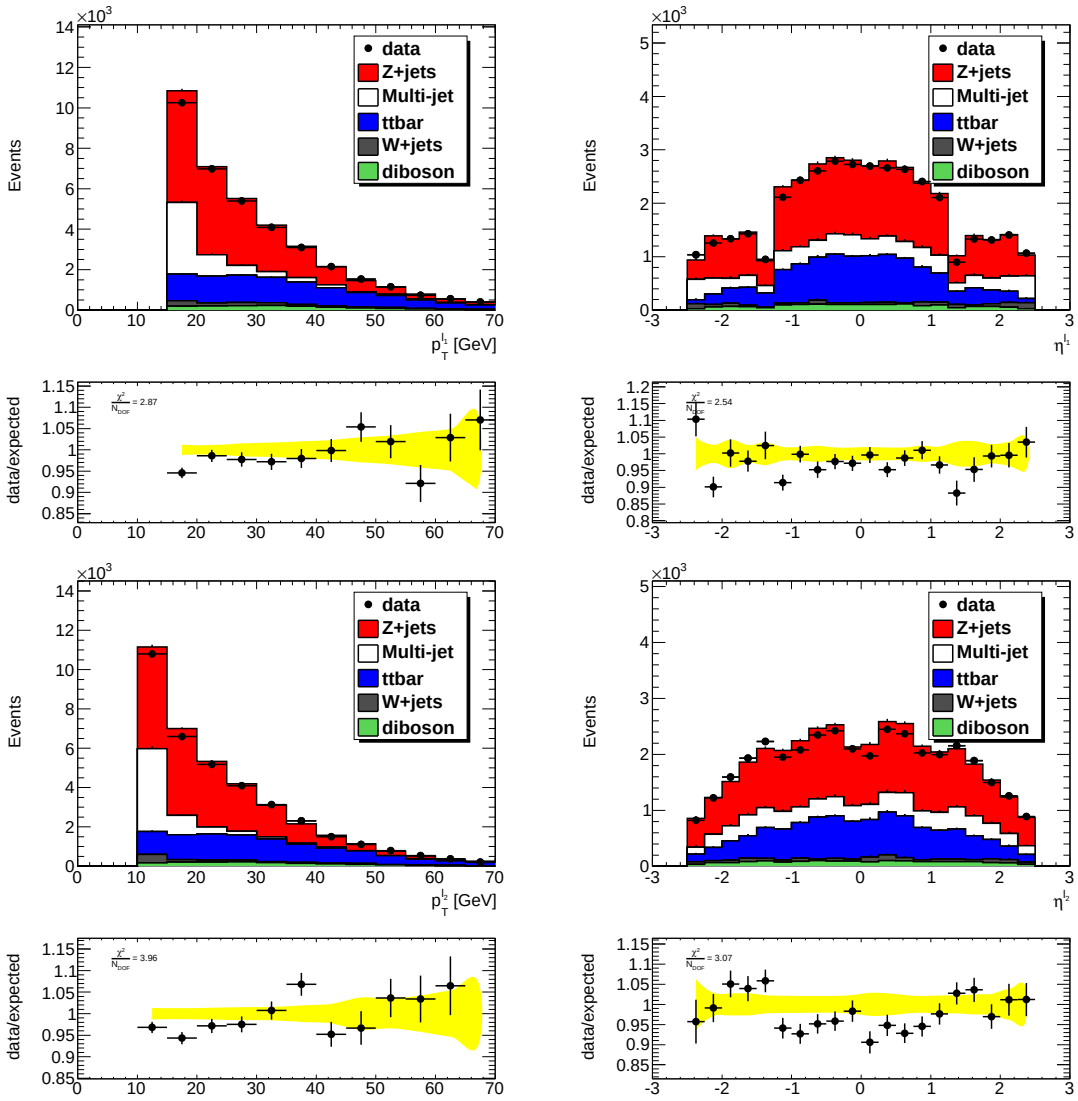

FIGURE 11. Kinematic distributions of leptons after basic selection. (Top) Electron kinematics. (Bottom) Muons kinematics.

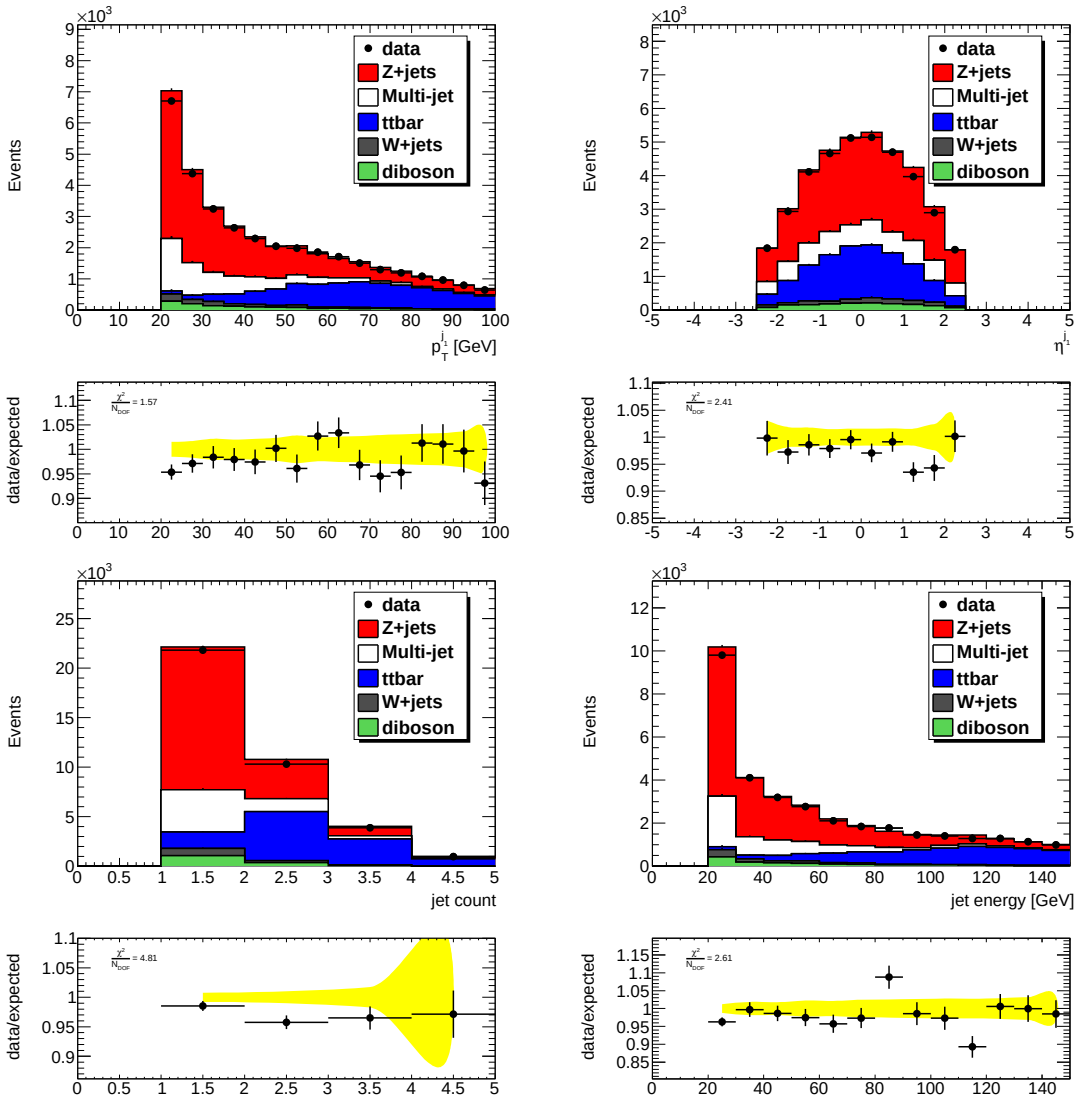

FIGURE 12. Jet related distributions after basic selection. (Top) Leading jet kinematics. (Bottom) Jet count and sum jet energy.

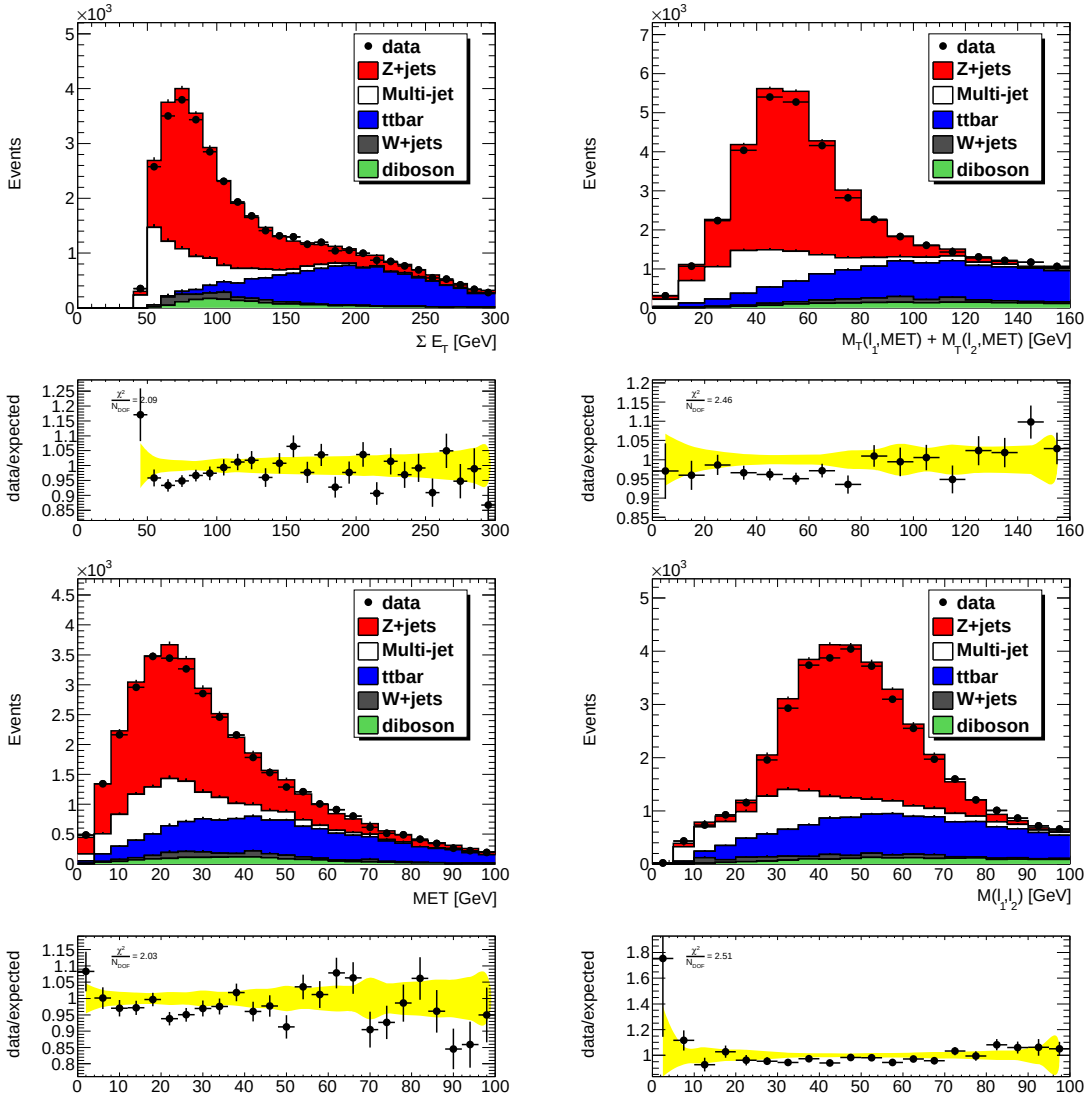

FIGURE 13. Event kinematics after basic selection. (Top) Scalar sum of transverse energy, sum of transverse mass. (Bottom) Missing transverse energy, lepton pair invariant mass.

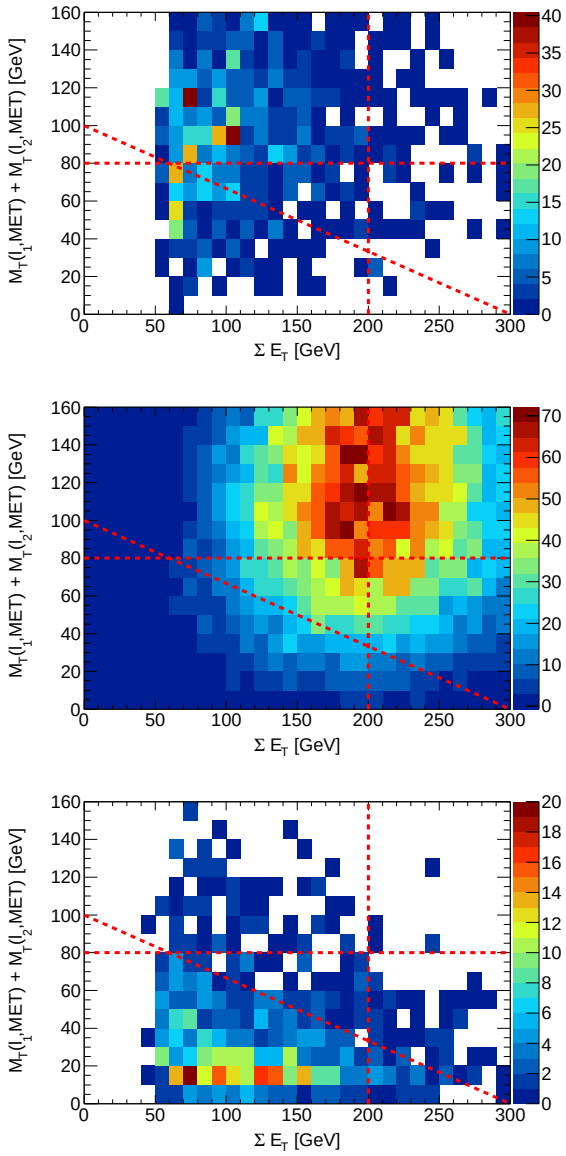

FIGURE 14. Event counts in the plane of sum $E_{\mathrm{T}} \times M_{\mathrm{T}}(\vec{E}_{\mathrm{T}}^{\mathrm{miss}}, \mu) + M_{\mathrm{T}}(\vec{E}_{\mathrm{T}}^{\mathrm{miss}}, \mathrm{e})$ after basic selection. (Top) W + jets. (Middle) $t\bar{t}$. (Bottom) Signal sample $M_{\Phi} = 30$ GeV. The dashed red line indicates the three requirements isolating signal in the bottom left quadrant of the plot.

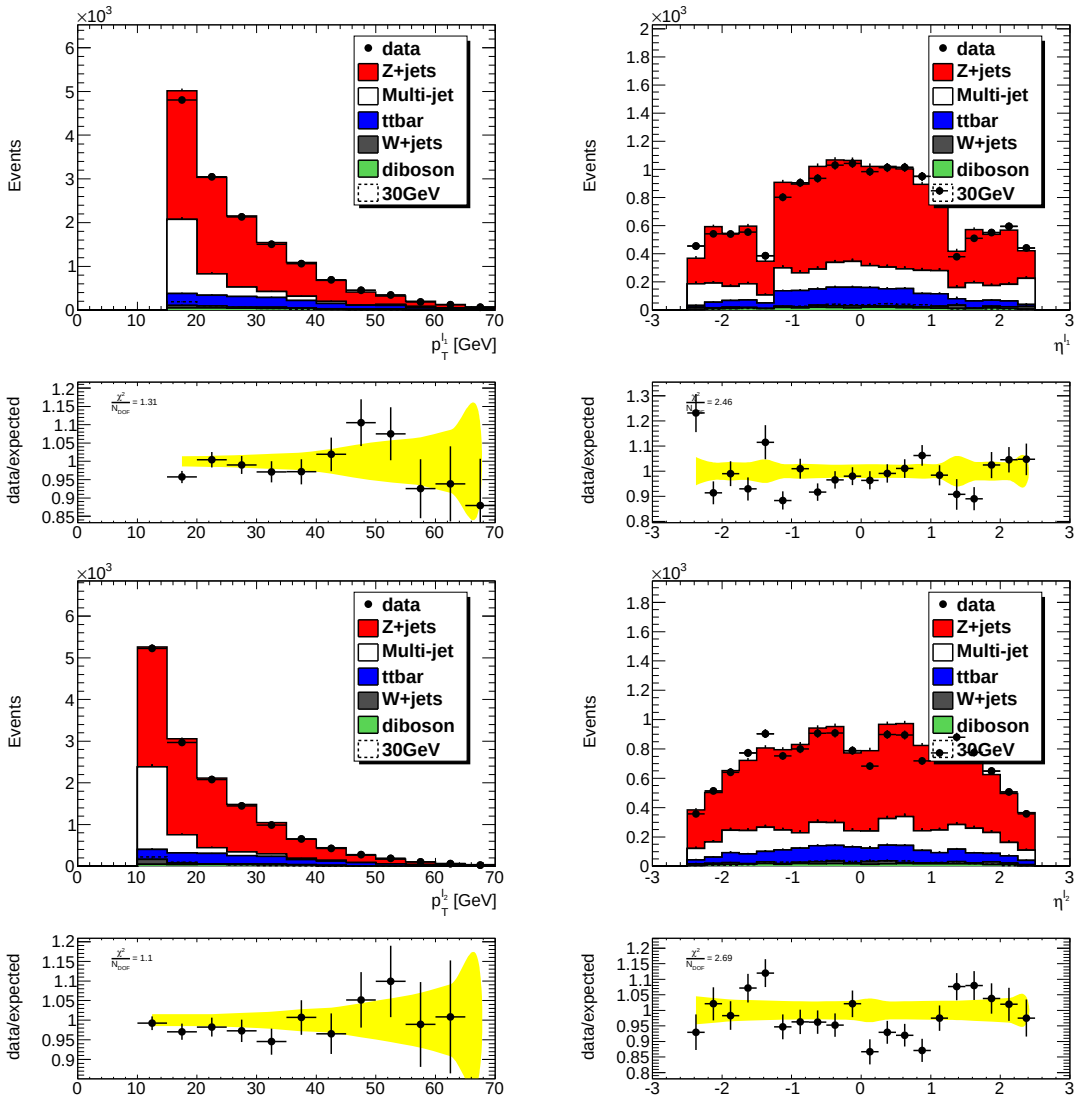

FIGURE 15. Kinematic distributions of leptons after Z+jets validation selection. (Top) Electron kinematics. (Bottom) Muons kinematics. Signal assumes $C_{b\bar{b}\Phi} = 5$.

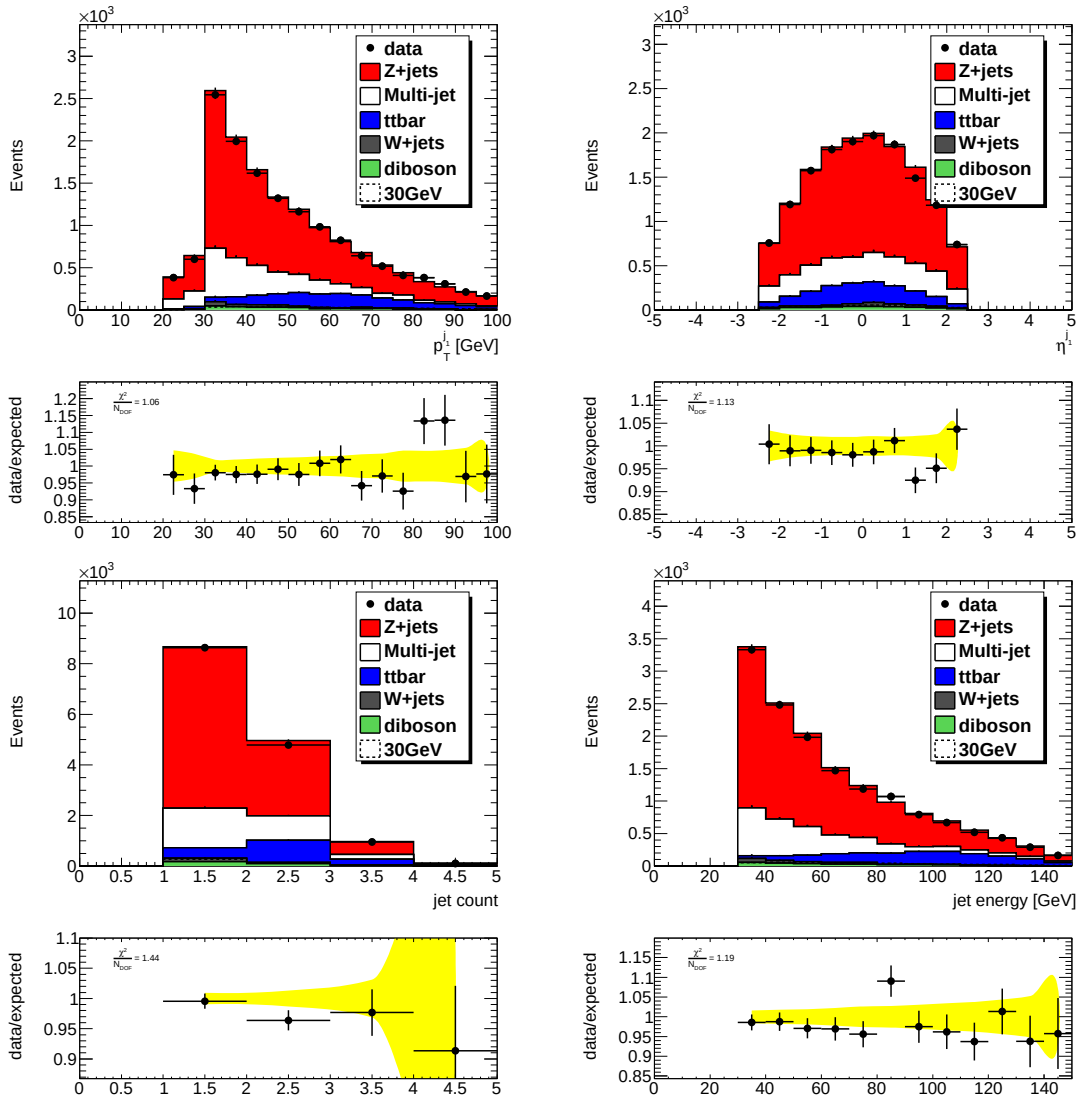

FIGURE 16. Jet related distributions after Z+jets validation selection. (Top) Leading jet kinematics. (Bottom) Jet count and sum jet energy. Signal assumes $C_{b\bar{b}\Phi} = 5$.

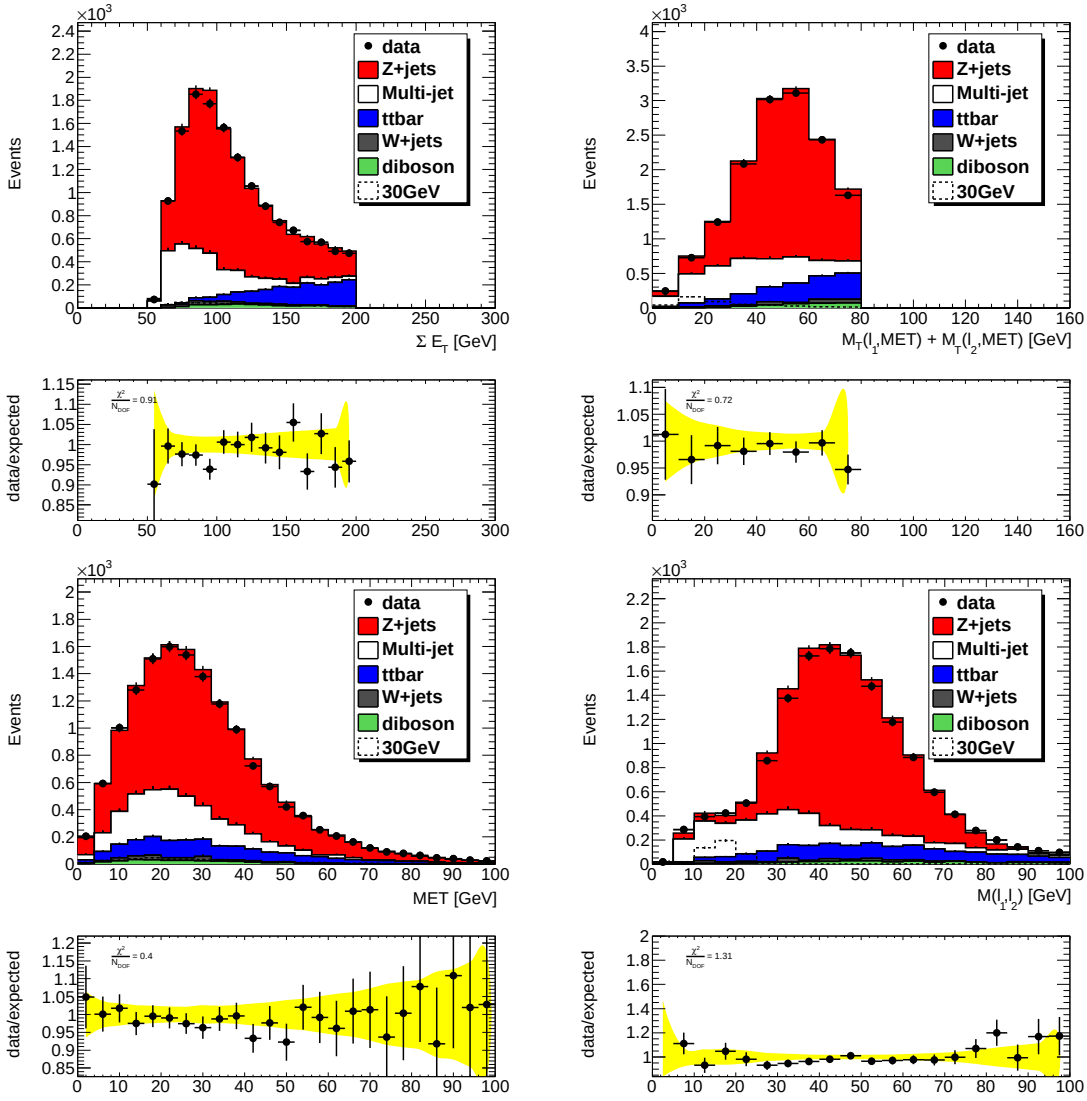

FIGURE 17. Event kinematics after Z+jets validation selection. (Top) Scalar sum of transverse energy, sum of transverse mass. (Bottom) Missing transverse energy, lepton pair invariant mass. Signal assumes $C_{b\bar{b}\Phi} = 5$.

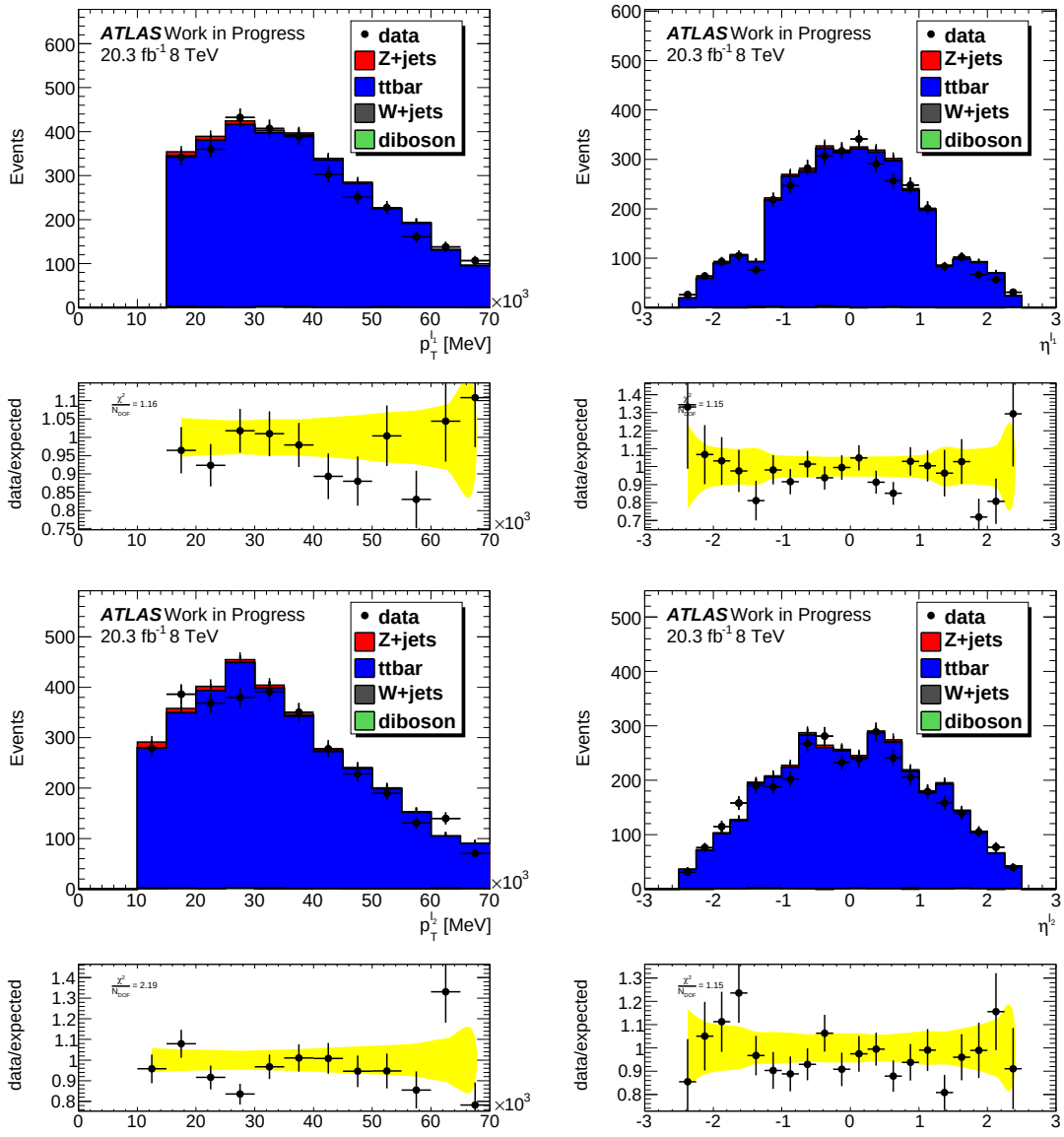

FIGURE 18. Kinematic distributions of leptons after $t\bar{t}$ validation selection. (Top) Electron kinematics. (Bottom) Muons kinematics.

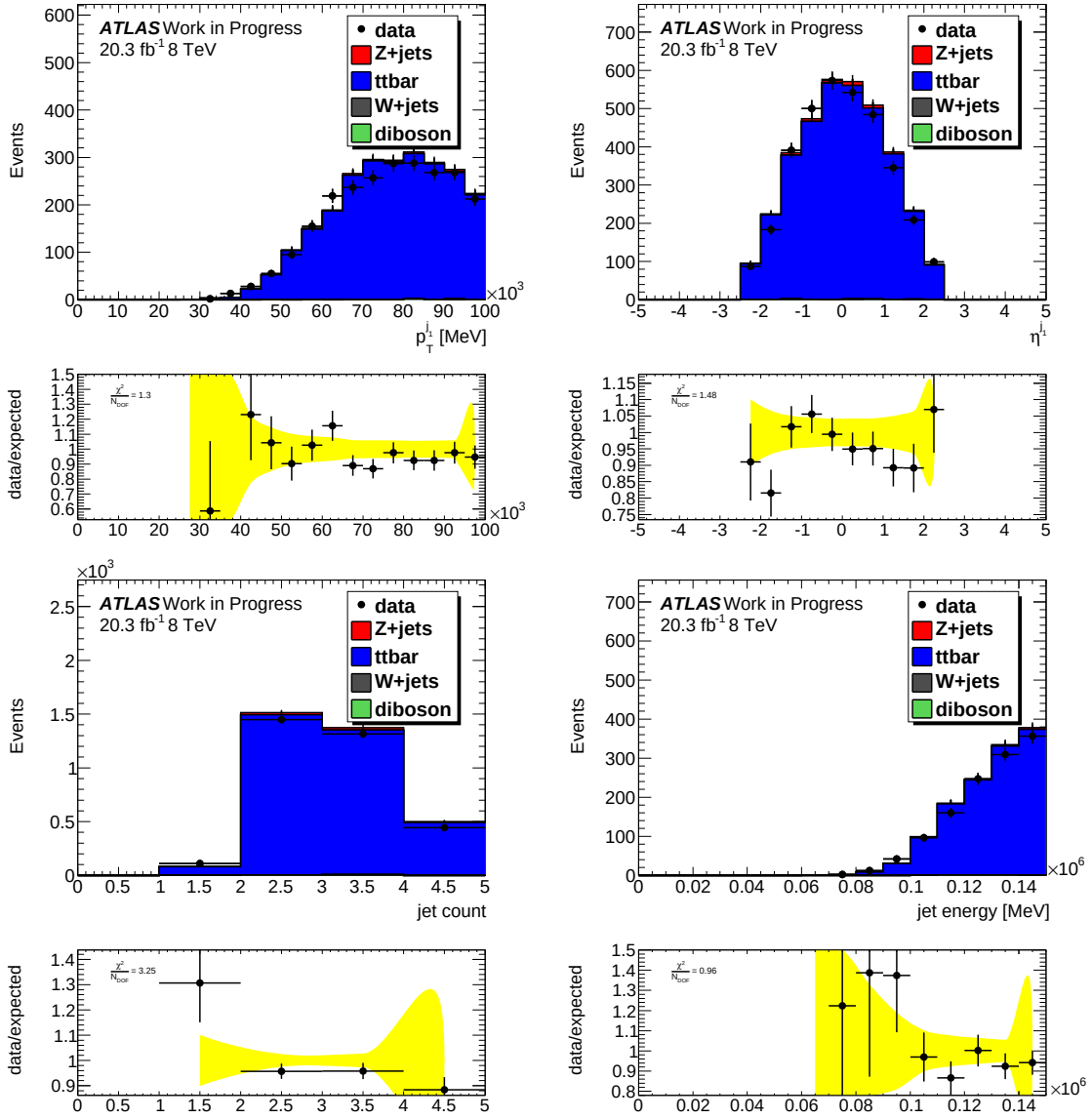

FIGURE 19. Jet related distributions after $t\bar{t}$ validation selection. (Top) Leading jet kinematics. (Bottom) Jet count and sum jet energy.

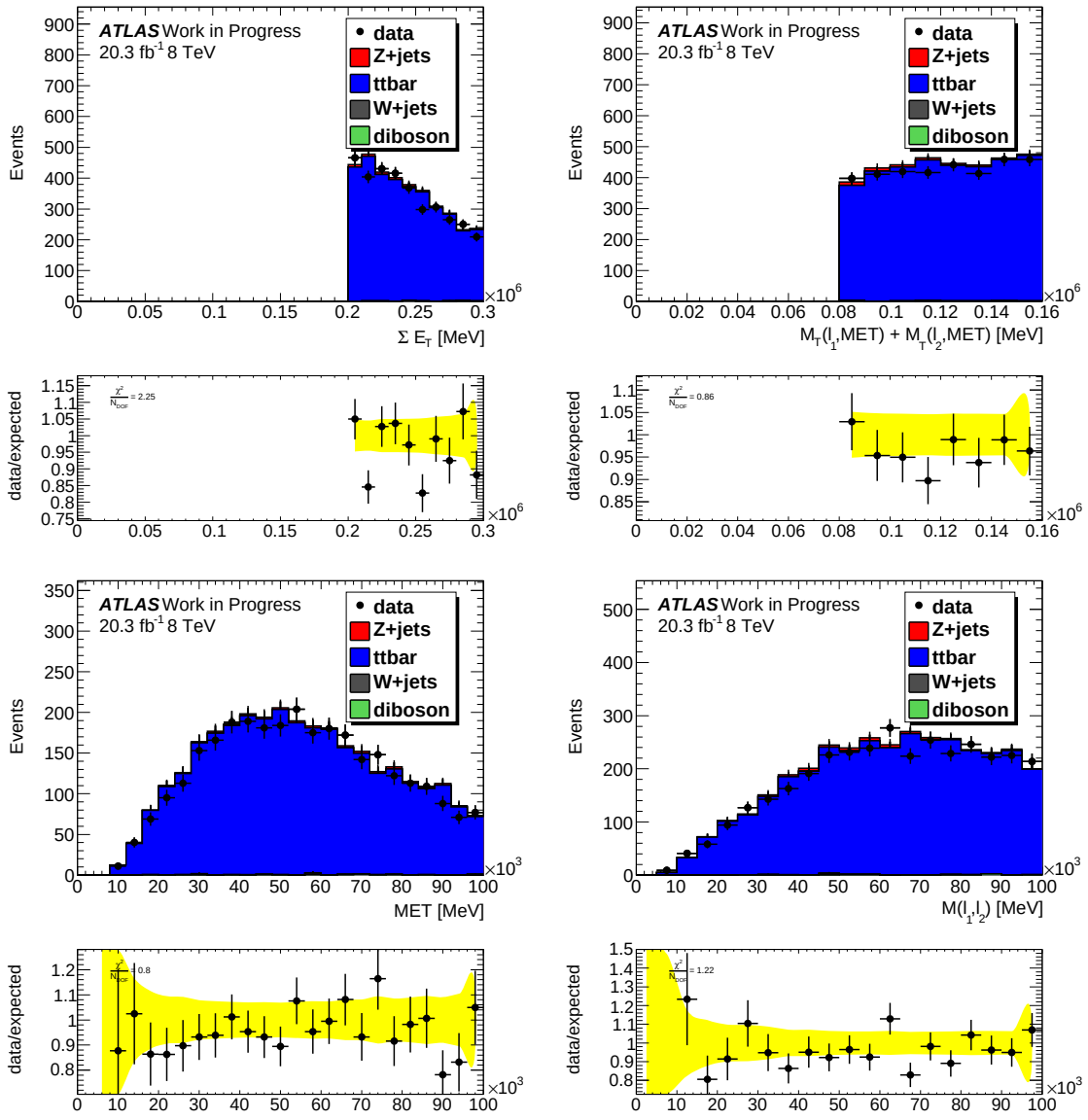

FIGURE 20. Event kinematics after $t\bar{t}$ validation selection. (Top) Scalar sum of transverse energy, sum of transverse mass. (Bottom) Missing transverse energy, lepton pair invariant mass.

QCD Multi-jet Validation

The QCD multi-jet validation selection makes all the same requirements as the Z+jets validation selection, except the electron is required to be `partially isolated`.

Requiring only partial isolation on the electron reduces the contribution of other SM processes and creates a fairly pure sample of QCD Multi-jet events which can be used to validate the data-driven estimation.

Event counts following the $t\bar{t}$ validation selection can be found in Table 11. A variety of distributions for events satisfying the QCD multi-jet validation selection are shown in Figures 21, 22 and 23.

Signal Selection

The signal selection makes all the same requirements as the Z+jets validation selection. In addition sum $E_{\mathrm{T}} + 3 \times (M_{\mathrm{T}}(\vec{E}_{\mathrm{T}}^{\mathrm{miss}}, \mathrm{muon}) + M_{\mathrm{T}}(\vec{E}_{\mathrm{T}}^{\mathrm{miss}}, \mathrm{electron})$ must be less than 300 GeV. Finally, at least one jet in the event must satisfy the bottom-tagging criteria.

Sample	Counts
$b\Phi(M_{\Phi}$=30 GeV)	53.96 ± 6.82
Z/γ^* + jets	1246.23 ± 8.55
QCD Multi-jet	6905.17 ± 169.88
$t\bar{t}$	195.9 ± 10.03
W + jets	156.51 ± 24.37
Diboson	25.9 ± 2.9
total SM	8529.71 ± 172.15
data	7904.0

TABLE 11. Event counts after QCD multi-jet validation selection. Backgrounds in red are estimated using data-driven techniques. Signal assumes $C_{b\bar{b}\Phi} = 5$.

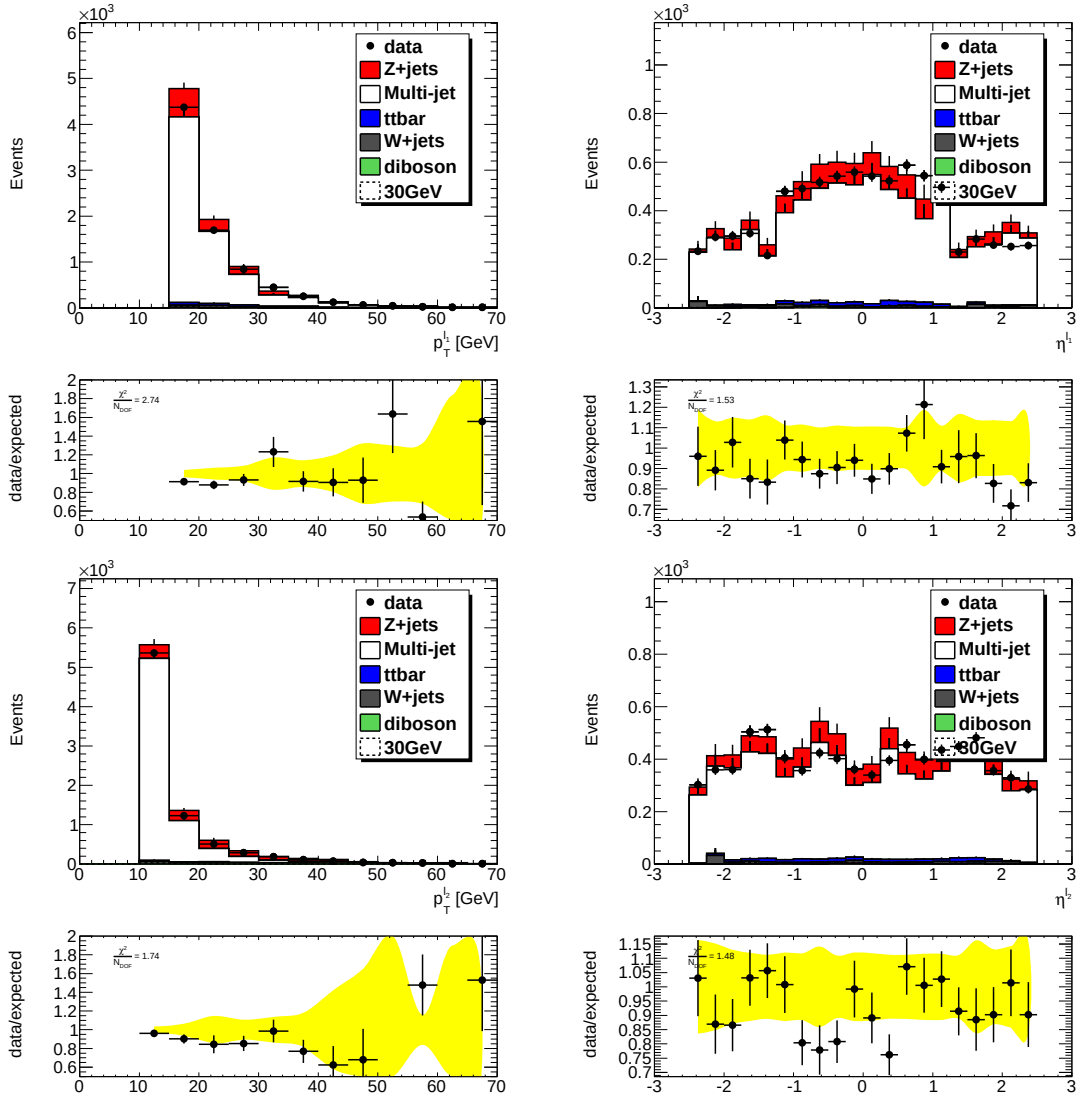

FIGURE 21. Kinematic distributions of leptons after QCD multi-jet validation selection. (Top) Electron kinematics. (Bottom) Muons kinematics. Signal assumes $C_{b\bar{b}\Phi} = 5$.

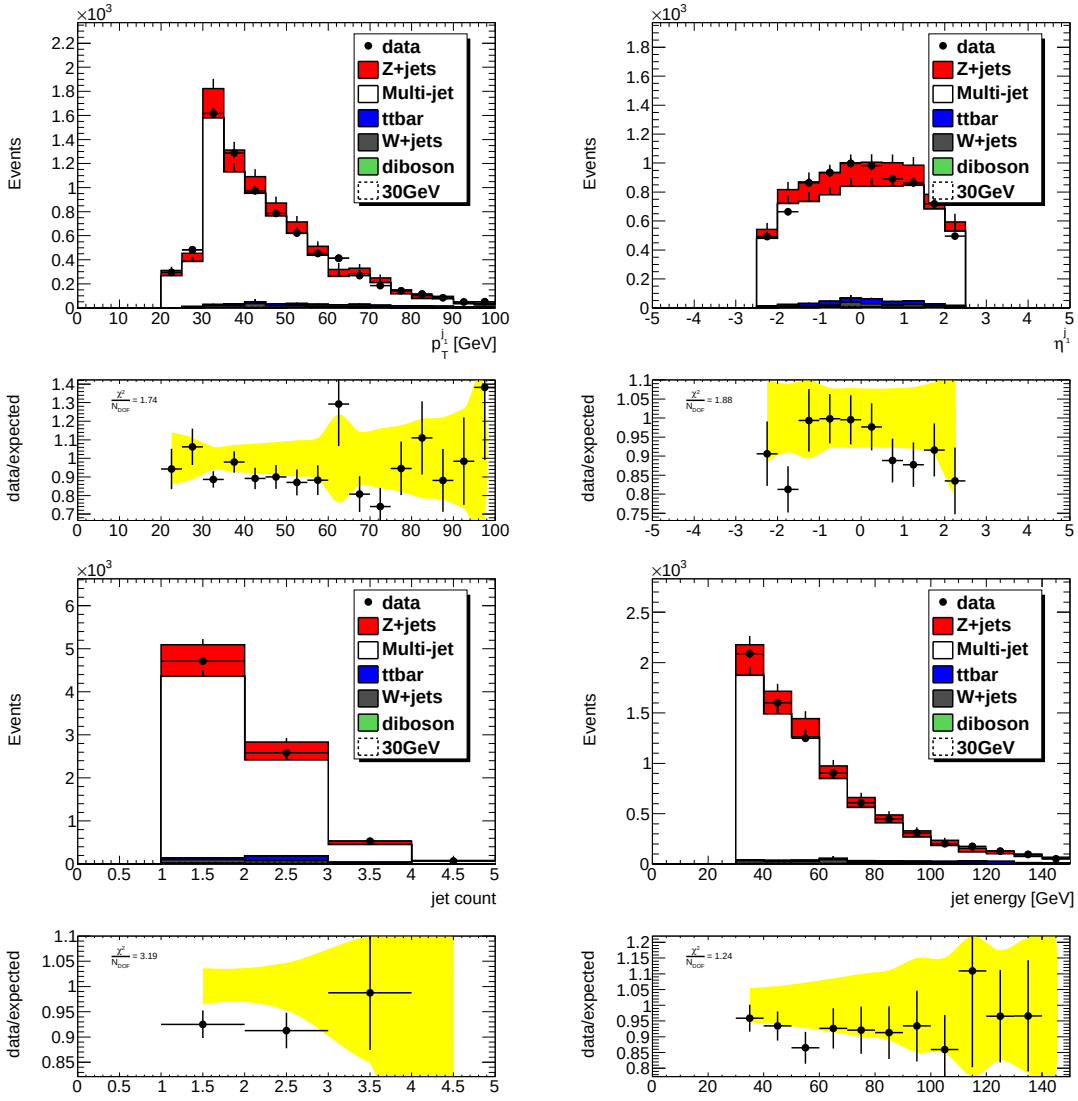

FIGURE 22. Jet related distributions after QCD multi-jet validation selection. (Top) Leading jet kinematics. (Bottom) Jet count and sum jet energy. Signal assumes $C_{b\bar{b}\Phi} = 5$.

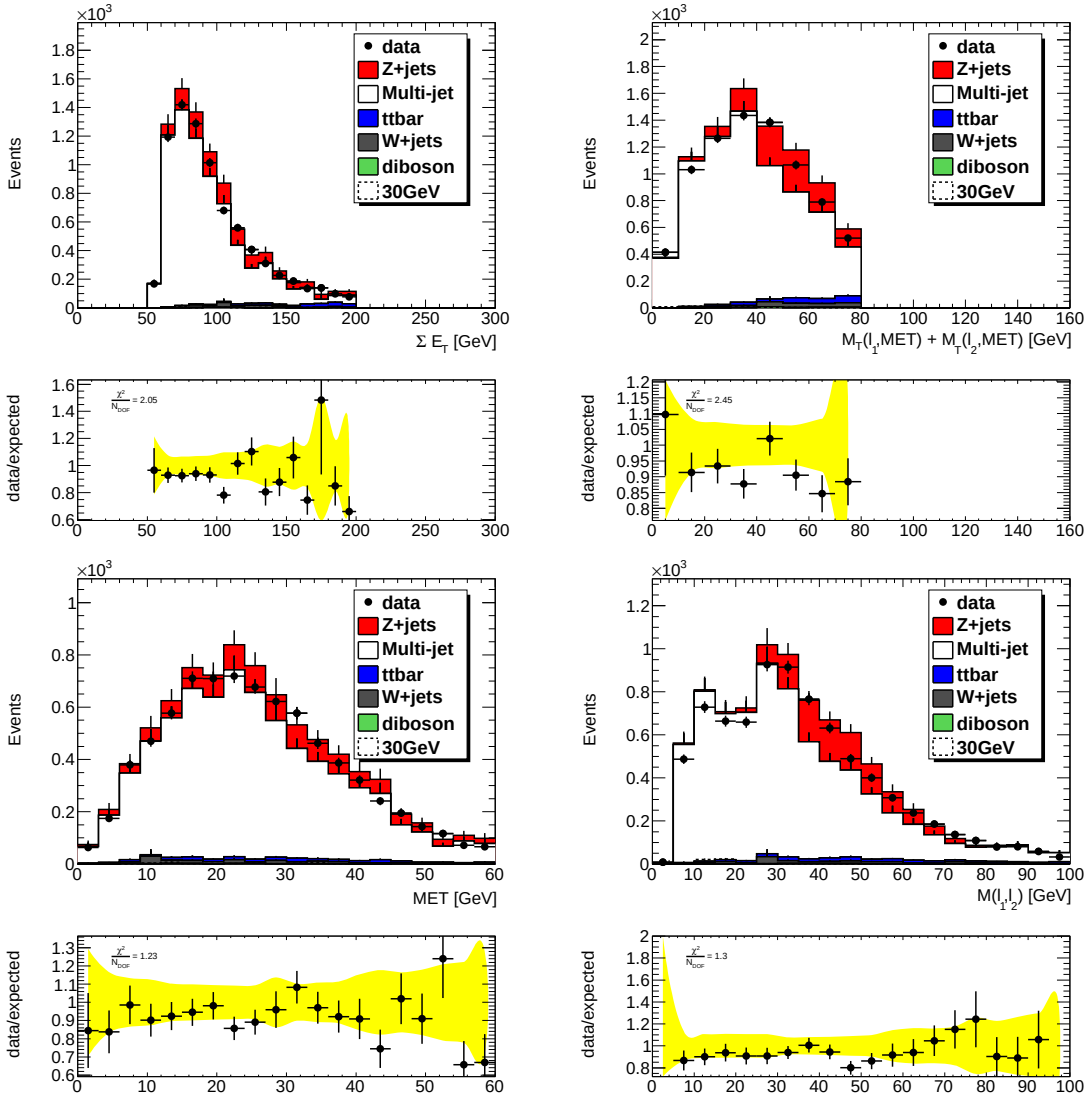

FIGURE 23. Event kinematics after QCD multi-jet validation selection. (Top) Scalar sum of transverse energy, sum of transverse mass. (Bottom) Missing transverse energy, lepton pair invariant mass. Signal assumes $C_{b\bar{b}\Phi} = 5$.

The first cut removes W+jets from one of the ABCD control regions while the bottom-tag reduces Z/γ^* + jets and QCD Multi-jet. Event counts following the signal selection can be found in Table 12. A variety of distributions for events satisfying the signal selection are shown in Figures 24, 25 and 26.

Systematic Uncertainty

Several systematic uncertainties, related to object modelling and identification, are considered. A summary of the effect of each uncertainty on each sample after the signal selection is shown in Table 13.

Trigger

The `EF_e12Tvh_medium1_mu8` trigger scale factor uncertainty is measured in two separate factors `EF_e12Tvh_medium1` [25] and `EF_mu8` [2]. These uncertainties are summed in quadrature to give the total trigger scale factor uncertainty, they are referred to in Table 13 as `trigger`.

Muons

The Muon Combined Performance Group provides muon momentum scale and resolution correction uncertainties for MC simulation as well as muon identification efficiency correction uncertainties [2]. In Table 13 muon momentum scale and resolution uncertainties are combined and referred to as `mu_pt`, the muon identification uncertainty is referred to as `mu_id`.

Sample	Counts
$b\Phi(M_\Phi$=20 GeV)	289.95 ± 11.83
$b\Phi(M_\Phi$=30 GeV)	271.32 ± 15.11
$b\Phi(M_\Phi$=50 GeV)	154.37 ± 11.76
$b\Phi(M_\Phi$=70 GeV)	175.68 ± 10.85
Z/γ^* + jets	377.71 ± 4.08
QCD Multi-jet	227.43 ± 23.76
$t\bar{t}$	395.74 ± 14.49
W + jets	7.11 ± 3.2
Diboson	4.3 ± 1.09
total SM	1012.3 ± 28.33
data	1071.0

TABLE 12. Event counts after signal selection. Backgrounds in red are estimated using data-driven techniques. Signal assumes $C_{b\bar{b}\Phi} = 5$.

Sample	`trigger`	`mu_pt`	`mu_id`	`el_pt`	`el_id`	`JES`	`b-tag`	`lumi`
$b\Phi(M_\Phi$=20 GeV)	2.7%	0.0%	0.3%	2.3%	4.2%	1.4%	6.3%	2.8%
$b\Phi(M_\Phi$=30 GeV)	2.7%	0.2%	0.2%	2.6%	3.8%	1.1%	6.3%	2.8%
$b\Phi(M_\Phi$=50 GeV)	2.6%	0.0%	0.2%	5.2%	3.6%	2.2%	6.6%	2.8%
$b\Phi(M_\Phi$=70 GeV)	2.6%	0.3%	0.2%	1.0%	3.6%	5.1%	7.3%	2.8%
Z/γ^* + jets	5.4%	0.0%	0.5%	2.6%	6.2%	-	-	-
QCD Multi-jet	1.0%	0.1%	0.0%	0.4%	1.0%	0.2%	1.0%	0.8%
$t\bar{t}$	2.6%	0.0%	0.2%	0.0%	2.6%	5.1%	8.0%	2.8%
W + jets	2.8%	0.0%	0.3%	0.5%	4.7%	0.0%	16.1%	2.8%
Diboson	2.6%	0.0%	0.2%	0.1%	1.8%	1.4%	14.0%	2.8%

TABLE 13. Summary of effect of systematic uncertainties on event counts after signal selection.

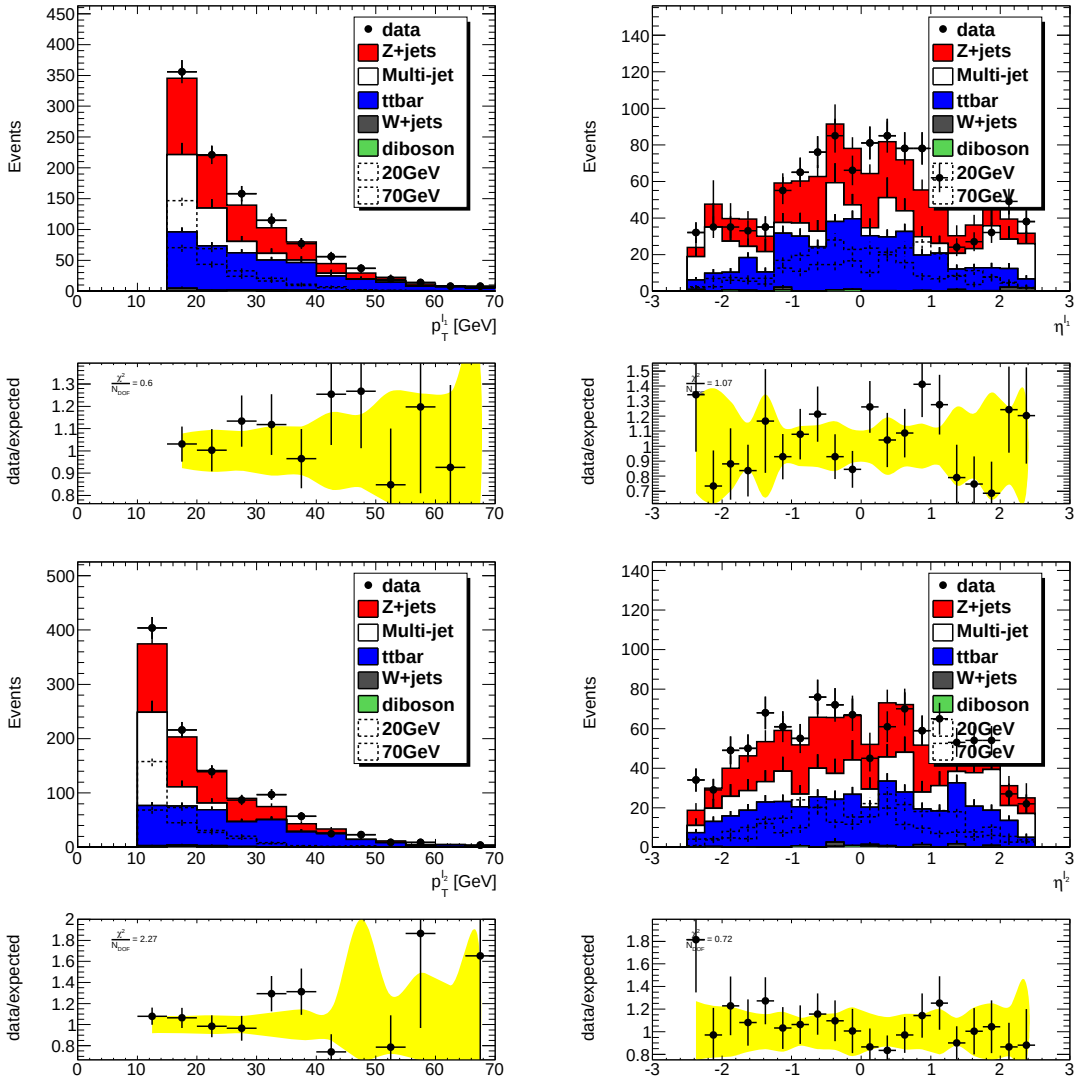

FIGURE 24. Kinematic distributions of leptons after signal selection. (Top) Electron kinematics. (Bottom) Muons kinematics. Signal assumes $C_{b\bar{b}\Phi} = 5$.

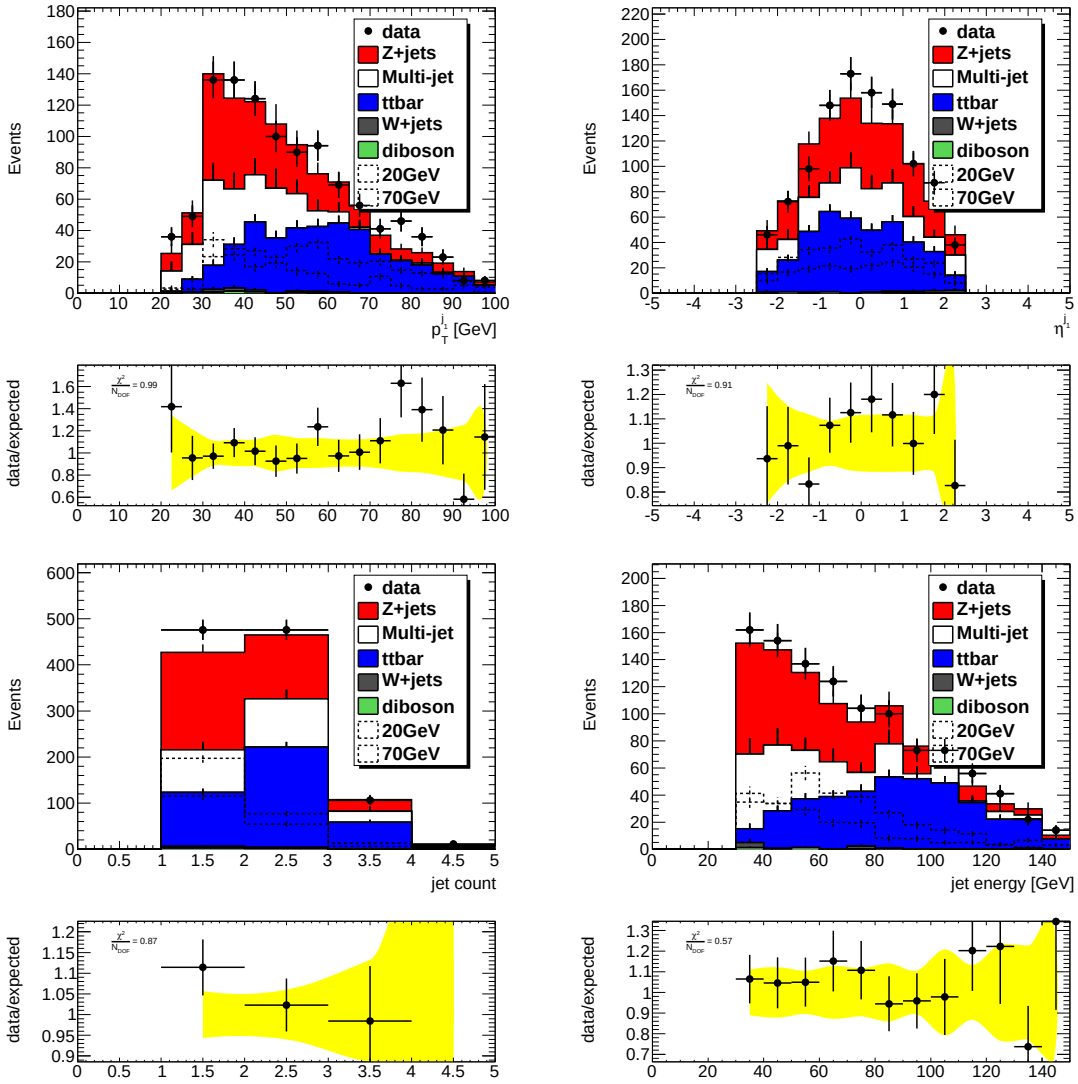

FIGURE 25. Jet related distributions after signal selection. (Top) Leading jet kinematics. (Bottom) Jet count and sum jet energy. Signal assumes $C_{bb\bar{\Phi}} = 5$.

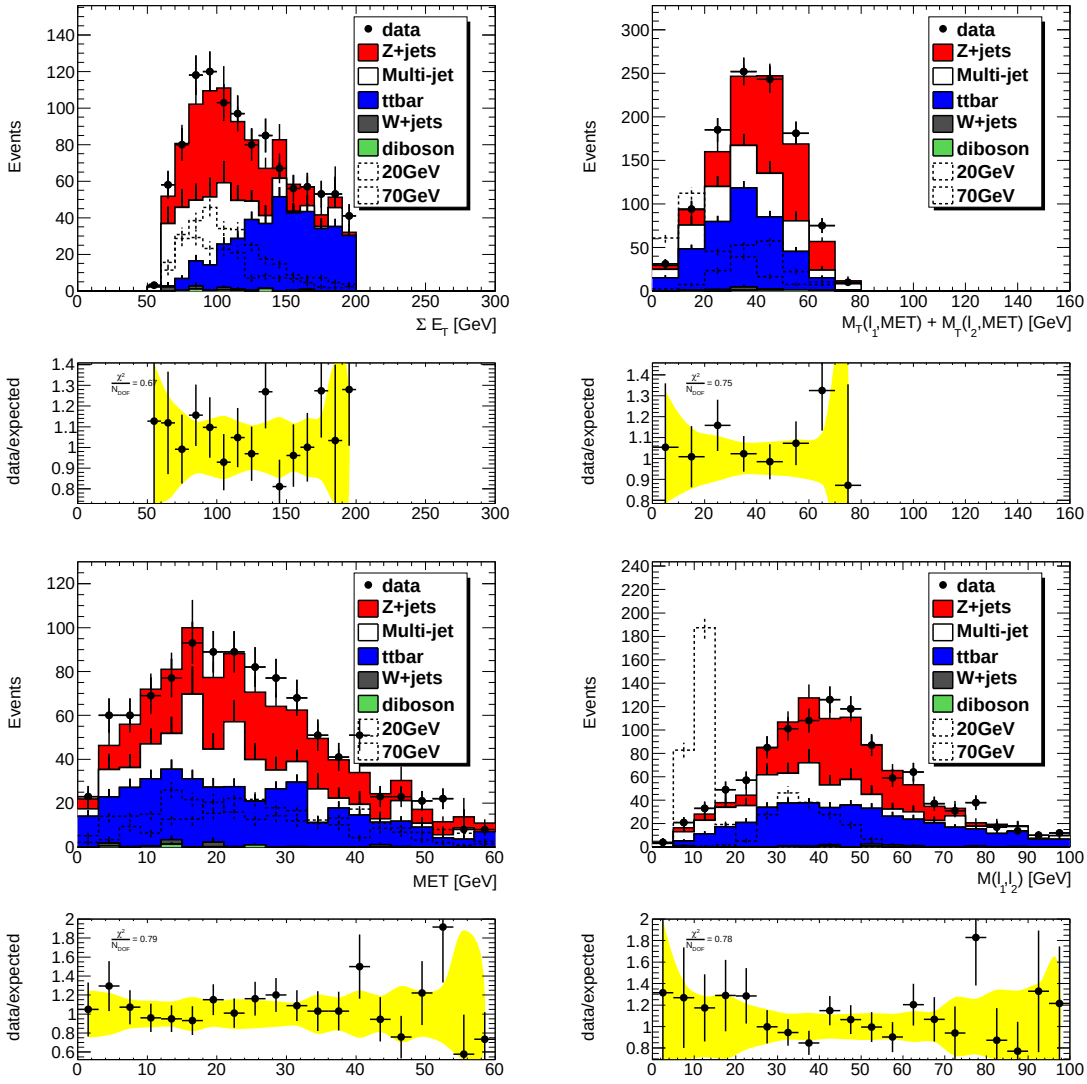

FIGURE 26. Event kinematics after signal selection. (Top) Scalar sum of transverse energy, sum of transverse mass. (Bottom) Missing transverse energy, lepton pair invariant mass. Signal assumes $C_{b\bar{b}\Phi} = 5$.

Electrons

The EGamma Performance Group provides electron energy scale and resolution correction uncertainties for MC simulation as well as electron identification efficiency correction uncertainties [25, 4]. In Table 13 electron energy scale and resolution uncertainties are combined and referred to as `el_pt`, the electron identification uncertainty is referred to as `el_id`.

Jets

The JetEtMiss Performance Group provides jet energy scale correction uncertainties [26] and jet energy resolution uncertainty [23]. There are fourteen independent jet energy scale uncertainties most which have only a small effect on event yields, these are combined along with the jet energy resolution uncertainty to create a total jet energy scale uncertainty referred to as `JES` in Table 13 .

The bottom-tagging efficiency correction uncertainty is also applied [3]. This uncertainty is referred to as `b-tag` in Table 13.

Luminosity

The uncertainty on the integrated luminosity is 2.8% [24], this uncertainty applies to simulated events. This uncertainty is referred to as `lumi` in Table 13.

Results

Observed Events

No visible excess is seen in Chapter 4.5. In order to set signal strength limits, per mass point, the signal selection is divided into mass bins. The mass bins

correspond to the 1σ width of the lepton pair invariant mass and is centered on the lepton pair invariant mass (approximately 50% of M_Φ). A scan is made in 5 GeV increments of M_Φ from 20 GeV to 70 GeV.

Signal samples for $M_\Phi \in \{20 \text{ GeV}, 30 \text{ GeV}, 50 \text{ GeV}, 70 \text{ GeV}\}$ are used to extrapolate expected signal event counts and uncertainties to mass bins without signal samples. A simple linear extrapolation is used for extrapolating the event counts and the systematic uncertainties.

In Table 14, event counts can be found for each mass window and including total uncertainty on signal and SM background.

Limit

Upper limits on signal strength are computed using a hybrid frequentist-baysian CL_s method [19].

The full likelihood for this single channel counting experiment is given by:

$$L(\mu, \{s', b'_i, \eta_j\}) = \text{Poisson}\big(n; \mu s + b\big)\, f(s'; s^{nom}, \sigma) \prod_i f(b'; b_i^{nom}, \sigma_i) \prod_j g(\eta_j)\,,$$

where μ represents the signal strength scale factor, n is the observed event count, i iterates of the backgrounds, $\{s', b'_i, \eta_j\}$ represent the set of nuisance parameters corresponding to the statistical uncertainty in signal and background ($\{s', b'_i\}$) and the systematic uncertainties ($\{\eta_j\}$). The statistical uncertainties are constrained by the functions f, where f is the log-normal distribution. The functions g are used to constrain the systematic uncertainties, where g is the normal distribution. The variation of signal and background yields (s, b_i) from systematic uncertainties are described by the functions $k^{syst}(\{\eta_j\})$ and $k_i^{syst}(\{\eta_j\})$. Polynomial interpolation

and exponential extrapolation are used to generate functions describing systematic uncertainties based on their estimated 1σ fluctuation.

The test statistic q_μ is defined

$$q_\mu \equiv -2ln\frac{L(\mu)}{L(\mu=0)}.$$

Pseudo-experiments are generated to determine the distribution of q_μ with $\mu = 0$ ($p(q_\mu|\mu = 0)$) and $\mu = \mu'$ ($p(q_\mu|\mu')$). The CL_s method [49] is used to determine upper limits on signal strength.

$$CL_s(\mu) \equiv \frac{\sum_{q_\mu=q_\mu^{obs}}^{\infty} p(q_\mu|\mu)}{\sum_{q_\mu=q_\mu^{obs}}^{\infty} p(q_\mu|0)}.$$

In order to set an upper limit on signal strength with 95%, the value of $\mu = \mu_{upper}$ satisfying $CL_s(\mu_{upper}) = 0.05$ is found.

The resulting 95% confidence upper limits on $C_{b\bar{b}\Phi}$ and fiducial cross-section multiplied by Φ branching ratio to di-tau as a function of Φ mass can be found in Figure 27.

Interpretation

The result in Figure 27 can be used to constrain suitable physics models. Although the analysis works with fiducial signal cross-sections, models may have different distributions of Φ p_T for which the selection efficiency is strongly dependent. In order to make this result relevant to many models, efficiencies as a function of Φ p_T are included in Table 15. These efficiencies can be used, along with the distribution of Φ p_T specific to the given model, to rescale the results found in Figure 27.

M_Φ	Signal	Signal Efficiency	total SM	observed
20 GeV	224.4±22.6	4.0%	39.4±9.5	41
25 GeV	202.9±21.9	3.9%	50.7±11.5	51
30 GeV	181.4±20.2	3.8%	58.4±13.0	69
35 GeV	159.6±18.7	3.6%	84.2±17.5	92
40 GeV	137.9±15.7	3.3%	104.1±15.2	118
45 GeV	116.1±15.1	2.9%	145.0±19.7	152
50 GeV	94.3±13.4	2.5%	182.9±19.5	202
55 GeV	100.5±13.8	2.8%	236.3±22.1	242
60 GeV	106.6±14.2	2.9%	291.3±25.0	274
65 GeV	112.8±14.7	3.1%	332.5±27.2	321
70 GeV	119.0±15.3	3.3%	356.7±28.6	355

TABLE 14. Event counts per mass window after signal selection. The uncertainty includes systematic and statistical uncertainty. Signal assumes $C_{b\bar{b}\Phi} = 5$.

M_Φ	0 - 40 GeV	40 - 60 GeV	60 - 80 GeV	80 - 100 GeV	$>$ 100 GeV
20 GeV	0.77%	4.03%	6.10%	6.83%	1.46%
30 GeV	0.97%	3.62%	5.56%	7.52%	4.50%
50 GeV	1.19%	3.01%	5.57%	5.21%	3.59%
70 GeV	1.96%	4.60%	6.90%	5.20%	3.76%

TABLE 15. Efficiency per mass point as a function of Φ p_T.

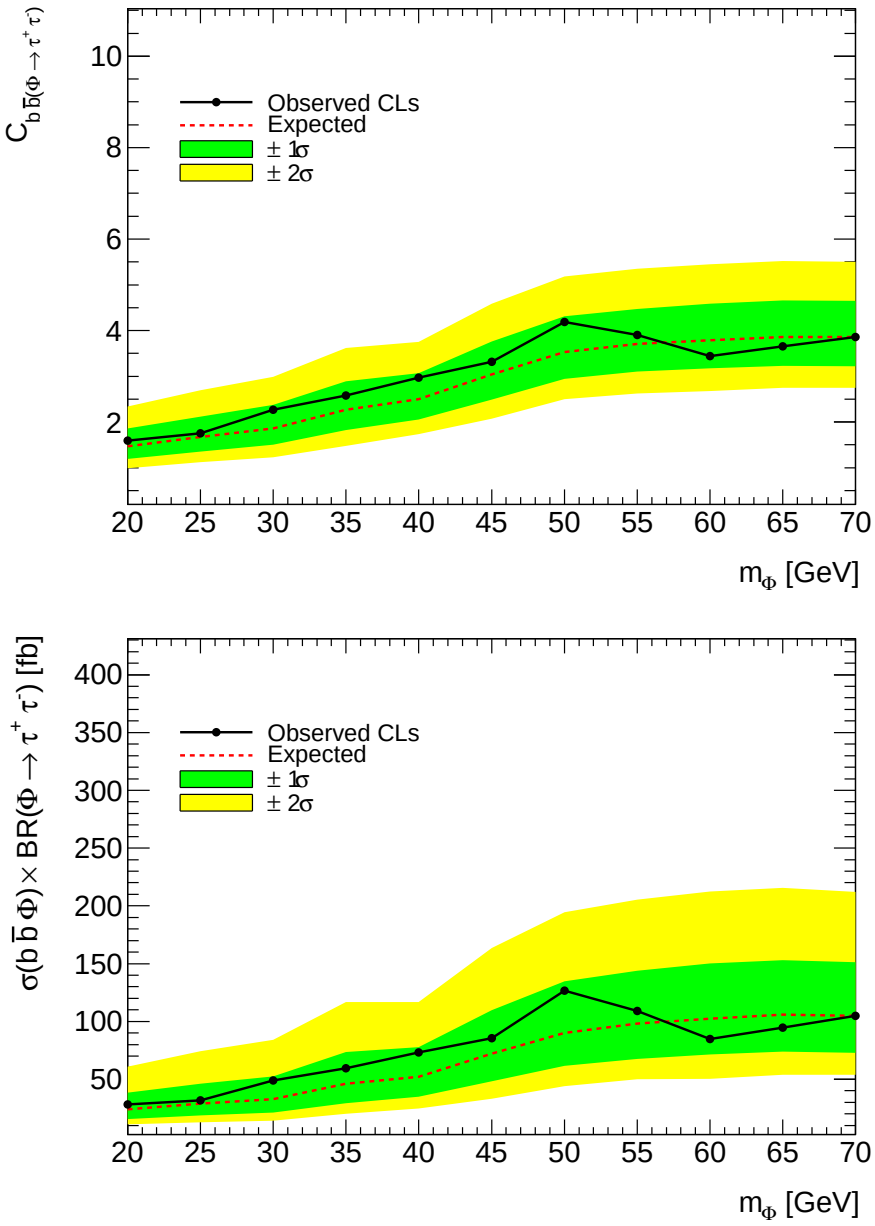

FIGURE 27. 95% confidence upper limits on $C_{b\bar{b}\Phi}$ (top) and fiducial cross-section multiplied by Φ branching ratio to di-tau (bottom)

CHAPTER V

CONCLUSION

A search for a new scalar boson produced in association with a bottom-quark and decaying to a pair of tau leptons has been conducted. This search used data corresponding to 20.3 fb^{-1} that was collected at the ATLAS experiment. No significant excess of the SM prediction was observed. Model independent 95% limits were produced as a function of the scalar boson mass. Limits were determined for the enhancement factor $C_{b\bar{b}(\Phi\to\tau^+\tau^-)}$ as well as fiducial cross-section times branching fraction. In the mass range between 20 and 70 GeV the 95% confidence limit on the fiducial cross-section times branching fraction is less than 140 fb.

Recommended Future Work

This analysis can be conducted at future LHC campaigns. To improve upon the current result a number of recommendations are made. The efficiency of this search for low p_T Φ is quite low due to the combined lepton trigger thresholds. These thresholds are required to limit the trigger rate, but they could be lowered if tighter requirements are placed on lepton identification or isolation. The isolation can not be made too tight otherwise the QCD multi-jet estimate will suffer. This search could also be conducted using different tau decay channels in which at least one tau decays hadronically. This would result in a much higher branching ratio and less energy loss with one less neutrino. The background estimation would be much different for such a search.

REFERENCES CITED

[1] Commissioning of the ATLAS high-performance b-tagging algorithms in the 7 TeV collision data. Technical Report ATLAS-CONF-2011-102, CERN, Geneva, Jul 2011.

[2] Muon reconstruction efficiency in reprocessed 2010 LHC proton-proton collision data recorded with the ATLAS detector. Technical Report ATLAS-CONF-2011-063, CERN, Geneva, Apr 2011.

[3] Measurement of the b-tag Efficiency in a Sample of Jets Containing Muons with 5 fb^{-1} of Data from the ATLAS Detector. Technical Report ATLAS-CONF-2012-043, CERN, Geneva, Mar 2012.

[4] Electron efficiency measurements with the ATLAS detector using the 2012 LHC proton-proton collision data. Technical Report ATLAS-CONF-2014-032, CERN, Geneva, Jun 2014.

[5] G. Aad et al. The ATLAS Experiment at the CERN Large Hadron Collider. *JINST*, 3:S08003, 2008.

[6] G. Aad et al. Expected Performance of the ATLAS Experiment - Detector, Trigger and Physics. 2009.

[7] Georges Aad et al. Observation of a new particle in the search for the Standard Model Higgs boson with the ATLAS detector at the LHC. *Phys. Lett.*, B716:1–29, 2012.

[8] J. Abdallah et al. Searches for neutral higgs bosons in extended models. *Eur. Phys. J.*, C38:1–28, 2004.

[9] P. A. R. Ade et al. Planck 2013 results. I. Overview of products and scientific results. *Astron. Astrophys.*, 571:A1, 2014.

[10] S. Agostinelli et al. GEANT4: A Simulation toolkit. *Nucl. Instrum. Meth.*, A506:250–303, 2003.

[11] A. Airapetian et al. ATLAS: Detector and physics performance technical design report. Volume 1. 1999.

[12] Simone Alioli, Sven-Olaf Moch, and Peter Uwer. Hadronic top-quark pair-production with one jet and parton showering, 2011.

[13] Elisabetta Barberio, Bob van Eijk, and Zbigniew Was. PHOTOS: A Universal Monte Carlo for QED radiative corrections in decays. *Comput. Phys. Commun.*, 66:115–128, 1991.

[14] Martin Bauer, Marcela Carena, and Katrin Gemmler. Creating the Fermion Mass Hierarchies with Multiple Higgs Bosons, 2015.

[15] Michael Benedikt, Paul Collier, V Mertens, John Poole, and Karlheinz Schindl. *LHC Design Report*. CERN, Geneva, 2004.

[16] Jeremy Bernon, John F. Gunion, Yun Jiang, and Sabine Kraml. Light Higgs bosons in Two-Higgs-Doublet Models. 2014.

[17] G. C. Branco, P. M. Ferreira, L. Lavoura, M. N. Rebelo, Marc Sher, and Joao P. Silva. Theory and phenomenology of two-Higgs-doublet models. *Phys. Rept.*, 516:1–102, 2012.

[18] Andy Buckley, Jonathan Butterworth, David Grellscheid, Hendrik Hoeth, Leif Lonnblad, James Monk, Holger Schulz, and Frank Siegert. Rivet user manual, 2010.

[19] Emmanuel Busato, David Calvet, and Timothe Theveneaux-Pelzer. OpTHyLiC: an Optimised Tool for Hybrid Limits Computation, 2015.

[20] Matteo Cacciari, Gavin P. Salam, and Gregory Soyez. The anti-kt jet clustering algorithm. JHEP 0804:063,2008, 2008.

[21] John M Campbell and R. K. Ellis. MCFM for the Tevatron and the LHC. Nucl.Phys.Proc.Suppl.205-206:10-15,2010, 2010.

[22] Serguei Chatrchyan et al. Observation of a new boson at a mass of 125 GeV with the CMS experiment at the LHC. *Phys. Lett.*, B716:30–61, 2012.

[23] ATLAS Collaboration. Jet energy resolution in proton-proton collisions at sqrt(s) = 7 TeV recorded in 2010 with the ATLAS detector. Eur. Phys. J. C, 73 3 (2013) 2306, 2012.

[24] ATLAS Collaboration. Improved luminosity determination in pp collisions at sqrt(s) = 7 TeV using the ATLAS detector at the LHC. Eur. Phys. J. C 73 (2013) 2518, 2013.

[25] ATLAS Collaboration. Electron reconstruction and identification efficiency measurements with the ATLAS detector using the 2011 LHC proton-proton collision data. Eur. Phys. J. C (2014) 74:2941, 2014.

[26] ATLAS Collaboration. Jet energy measurement and its systematic uncertainty in proton-proton collisions at $\sqrt{s} = 7$ TeV with the ATLAS detector. Eur. Phys. J. C (2015) 75:17, 2014.

[27] ATLAS Collaboration. Measurement of the muon reconstruction performance of the ATLAS detector using 2011 and 2012 LHC proton-proton collision data. 2014.

[28] ATLAS Collaboration. Performance of the ATLAS muon trigger in pp collisions at $\sqrt{s} = 8$ TeV. 2014.

[29] The ATLAS Collaboration and G. Aad. Expected Performance of the ATLAS Experiment - Detector, Trigger and Physics, 2008.

[30] The ATLAS TRT collaboration. The ATLAS Transition Radiation Tracker (TRT) proportional drift tube: design and performance. *Journal of Instrumentation*, 3(02):P02013, 2008.

[31] John C. Collins, Davison E. Soper, and George F. Sterman. Factorization of Hard Processes in QCD. *Adv. Ser. Direct. High Energy Phys.*, 5:1–91, 1989.

[32] Gennaro Corcella, Ian G. Knowles, Giuseppe Marchesini, Stefano Moretti, Kosuke Odagiri, Peter Richardson, Michael H. Seymour, and Bryan R. Webber. HERWIG 6: an event generator for hadron emission reactions with interfering gluons (including supersymmetric processes). *Journal of High Energy Physics*, 2001(01):010, 2001.

[33] G. Duckeck, D. Barberis, R. Hawkings, R. Jones, N. McCubbin, G. Poulard, D. Quarrie, T. Wenaus, and E. Obreshkov. ATLAS computing: Technical design report. 2005.

[34] F. Englert and R. Brout. Broken Symmetry and the Mass of Gauge Vector Mesons. *Phys. Rev. Lett.*, 13:321–323, Aug 1964.

[35] T. Gleisberg, S. Hoeche, F. Krauss, M. Schoenherr, S. Schumann, F. Siegert, and J. Winter. Event generation with SHERPA 1.1. JHEP 0902:007,2009, 2008.

[36] D. Griffiths. *Introduction to Elementary Particles*. Physics textbook. Wiley, 2008.

[37] Peter W. Higgs. Broken Symmetries and the Masses of Gauge Bosons. *Phys. Rev. Lett.*, 13:508–509, Oct 1964.

[38] Stanislaw Jadach, Johann H. Kuhn, and Zbigniew Was. TAUOLA: A Library of Monte Carlo programs to simulate decays of polarized tau leptons. *Comput. Phys. Commun.*, 64:275–299, 1990.

[39] Rudolph Emil Kalman. A New Approach to Linear Filtering and Prediction Problems. *Transactions of the ASME–Journal of Basic Engineering*, 82(Series D):35–45, 1960.

[40] Christopher F. Kolda and Hitoshi Murayama. The Higgs mass and new physics scales in the minimal standard model. *JHEP*, 07:035, 2000.

[41] Hung-Liang Lai, Marco Guzzi, Joey Huston, Zhao Li, Pavel M. Nadolsky, Jon Pumplin, and C. P. Yuan. New parton distributions for collider physics. Phys.Rev.D82:074024,2010, 2010.

[42] W Lampl, S Laplace, D Lelas, P Loch, H Ma, S Menke, S Rajagopalan, D Rousseau, S Snyder, and G Unal. Calorimeter Clustering Algorithms: Description and Performance. Technical Report ATL-LARG-PUB-2008-002. ATL-COM-LARG-2008-003, CERN, Geneva, Apr 2008.

[43] A Loginov. Strategies of data-driven estimations of ttbar backgrounds in ATLAS. Technical Report ATL-PHYS-PROC-2010-067, CERN, Geneva, Aug 2010.

[44] Michelangelo L. Mangano, Mauro Moretti, Fulvio Piccinini, Roberto Pittau, and Antonio D. Polosa. ALPGEN, a generator for hard multiparton processes in hadronic collisions. *JHEP*, 07:001, 2003.

[45] Stephen P. Martin. A Supersymmetry primer. 1997. [Adv. Ser. Direct. High Energy Phys.18,1(1998)].

[46] K Nakamura and Particle Data Group. Review of Particle Physics. *Journal of Physics G: Nuclear and Particle Physics*, 37(7A):075021, 2010.

[47] ATLAS Outreach. ATLAS Fact Sheet : To raise awareness of the ATLAS detector and collaboration on the LHC. 2010.

[48] G Pasztor, D Damazio, and F Monticelli. Electron and photon trigger performance plots using 2012 data. Technical Report ATL-COM-DAQ-2014-058, CERN, Geneva, Jun 2014.

[49] A L Read. Presentation of search results: the CLs technique. *Journal of Physics G: Nuclear and Particle Physics*, 28(10):2693, 2002.

[50] Matts Roos. Astrophysical and cosmological probes of dark matter. 2012.

[51] Torbjorn Sjostrand, Stephen Mrenna, and Peter Z. Skands. PYTHIA 6.4 Physics and Manual. *JHEP*, 05:026, 2006.

[52] C. N. Yang and R. L. Mills. Conservation of isotopic spin and isotopic gauge invariance. *Phys. Rev.*, 96:191–195, Oct 1954.